ACSNANO
www.acsnano.org
ARTICLE

In-Plane Optical Anisotropy of Layered Gallium Telluride

Shengxi Huang,[†] Yuki Tatsumi,[‡] Xi Ling,[*,†] Huaihong Guo,[§] Ziqiang Wang,[∥] Garrett Watson,[⊥] Alexander A. Puretzky,[#] David B. Geohegan,[#] Jing Kong,[†] Ju Li,[∥] Teng Yang,[▽,‡] Riichiro Saito,[‡] and Mildred S. Dresselhaus[*,†,⊥]

[†]Department of Electrical Engineering and Computer Science, Massachusetts Institute of Technology, Cambridge, Massachusetts 02139, United States

[‡]Department of Physics, Tohoku University, Sendai 980-8578, Japan

[§]College of Sciences, Liaoning Shihua University, Fushun 113001, China

[∥]Department of Nuclear Science and Engineering, Massachusetts Institute of Technology, Cambridge, Massachusetts 02139, United States

[⊥]Department of Physics, Massachusetts Institute of Technology, Cambridge, Massachusetts 02139, United States

[#]Center for Nanophase Materials Sciences, Oak Ridge National Laboratory, Oak Ridge, Tennessee 37831, United States

[▽]Shenyang National Laboratory for Materials Science, Institute of Metal Research, Chinese Academy of Sciences, Shenyang 110016, China

Supporting Information

ABSTRACT: **Layered gallium telluride (GaTe) has attracted much attention recently, due to its extremely high photoresponsivity, short response time, and promising thermoelectric performance. Different from most commonly studied two-dimensional (2D) materials, GaTe has in-plane anisotropy and a low symmetry with the C_{2h}^3 space group. Investigating the in-plane optical anisotropy, including the electron−photon and electron−phonon interactions of GaTe is essential in realizing its applications in optoelectronics and thermoelectrics. In this work, the anisotropic light-matter interactions in the low-symmetry material GaTe are studied using anisotropic optical extinction and Raman spectroscopies as probes. Our polarized optical extinction spectroscopy reveals the weak anisotropy in optical extinction spectra for visible light of multilayer GaTe. Polarized Raman spectroscopy proves to be sensitive to the crystalline orientation of GaTe, and shows the intricate dependences of Raman anisotropy on flake thickness, photon and phonon energies. Such intricate dependences can be explained by theoretical analyses employing first-principles calculations and group theory. These studies are a crucial step toward the applications of GaTe especially in optoelectronics and thermoelectrics, and provide a general methodology for the study of the anisotropy of light-matter interactions in 2D layered materials with in-plane anisotropy.**

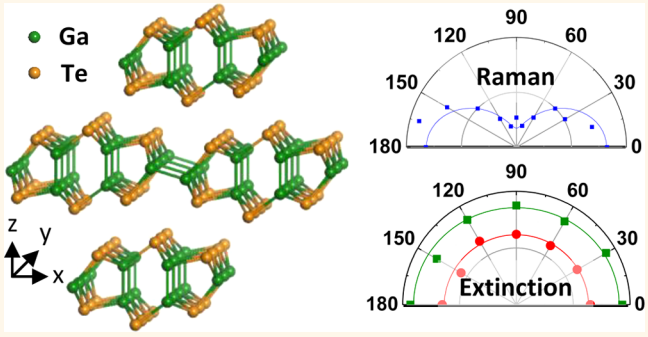

KEYWORDS: *light-matter interaction, electron−photon interaction, polarization-dependent Raman spectroscopy, polarization-dependent optical extinction, group theory, optical transition selection rules*

Two-dimensional (2D) materials constitute a large family with various members from the ones with high in-plane symmetry, such as graphene, to those with low in-plane symmetry, such as black phosphorus (BP), gallium telluride (GaTe), tin selenide (SnSe) and rhenium disulfide (ReS_2).[1−5] These materials show diverse optical and electrical properties depending on their structures.[6−11] In particular, low-symmetry 2D materials show significant in-plane anisotropy in their electrical, optical and thermal properties. For example, compared to the D_{6h} symmetry of graphene, the reduced symmetry (D_{2h}) of BP has been reported to result in the mobility,[12] photoemission,[8] and thermoelectric ZT factor[13,14] being larger along the armchair direction than along the zigzag direction. In our recent research,[15] we used spectroscopic techniques to reveal the anisotropic light-matter interactions in

Received: July 26, 2016
Accepted: August 16, 2016
Published: August 16, 2016

DOI: 10.1021/acsnano.6b05002
ACS Nano 2016, 10, 8964−8972

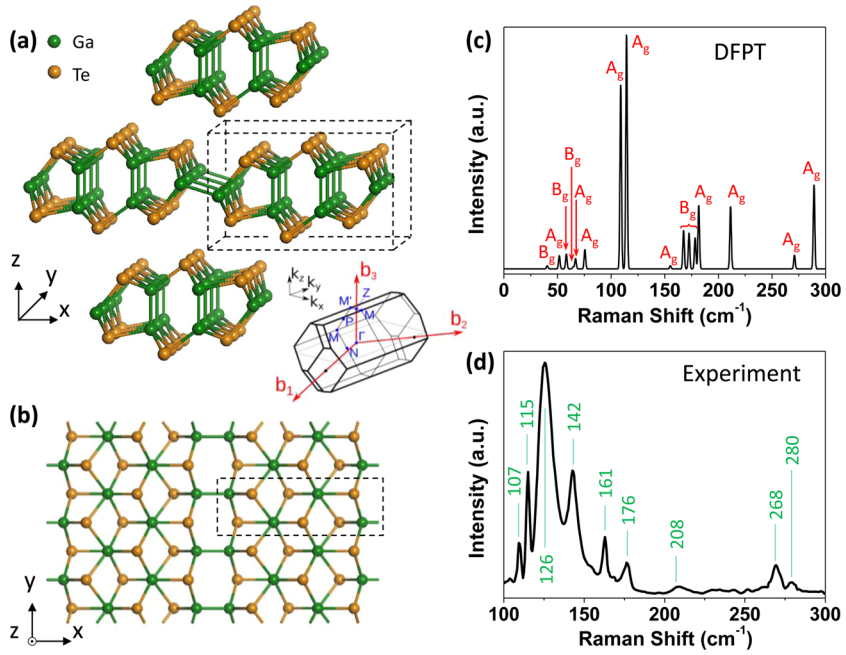

Figure 1. Crystal structure and Raman spectra of layered GaTe. (a) Front view for the crystal structure of bulk GaTe. (b) Top view for monolayer GaTe. The black dashed boxes in (a) and (b) correspond to the same group of atoms. Inset of (a): Brillouin zone for the primitive unit cell of bulk GaTe. (c) Calculated nonresonant Raman spectrum of bulk GaTe by DFPT methods. The symmetry of each mode is labeled. (d) Experimental Raman spectrum of a 125 nm thick GaTe flake at room temperature and under vacuum (10^{-5} mbar). The measurement was performed with 532 nm laser excitation. The peak frequencies are shown in units of cm^{-1}.

BP, including electron−photon and electron−phonon interactions, which indicates that it is crucial to understand the detailed anisotropy before applying the low-symmetry layered material to practical applications.[6,10,12,16,17]

As one of the important members among low-symmetry layered materials, GaTe has gained increasing attention in recent years.[18−28] With a direct bandgap of ∼1.7 eV for thicknesses ranging from few-layer to bulk, GaTe has demonstrated extremely high photoresponsivity (10^4 A/W) and a short response time (6 ms) in photodetectors,[20] and also promising potentials in various other photonic applications such as solar cells, imaging arrays, radiation detectors, nonlinear optics,[22,27,29] as well as in thermoelectric devices.[30,31] Although the in-plane anisotropic performance of those properties has been observed,[2,24,32] the reason behind, as well as a convenient spectroscopic identification of the crystalline orientation, are still under exploration.

In this work, we report the in-plane optical anisotropy in the low-symmetry layered material GaTe, including its anisotropic optical absorption, optical extinction and Raman scattering, which reveal anisotropic light-matter interactions. We found that a GaTe multilayer shows a weak anisotropy of optical absorption and extinction in the visible spectral range, but Raman intensity shows a strong dependence on crystalline orientation. These experimental observations can be explained by first-principles calculations and group theory analyses. Moreover, due to the thickness dependence of the energy band structure and the symmetry of each energy level, the anisotropies of the Raman intensity show an intricate dependence on flake thickness, photon and phonon energies, which can be explained by group theory and optical transition selection rules. This work provides important guidelines for the design of optoelectronic and thermoelectric devices made of GaTe, and presents a general methodology for the study of optical anisotropy in layered materials with in-plane anisotropy.

RESULTS AND DISCUSSION

Bulk GaTe is a layered material with monoclinic structure as shown in Figure 1(a,b), which consists of 6 Ga and 6 Te atoms in the primitive unit cell. The adjacent GaTe layers are stacked to each other in the *z*-direction by van der Waals forces. Bulk GaTe has C_{2h}^3 ($C2/m$) symmetry,[20,33,34] which has a 2-fold rotational axis C_2 (*y*-axis) and a mirror plane σ_h (*x*−*z* plane). The inset in Figure 1(a) illustrates the Brillouin zone with several high-symmetry points ***Γ***, ***M***, ***Z***, ***M′***, ***P*** and ***N***. According to our density functional theory (DFT) calculations (Figure S1), a direct bandgap is located at the ***Z*** point (E_g = 1.65 eV) and slightly larger bandgaps can be seen at the ***P*** or ***M*** point (E_g = 1.80 eV), which is consistent with the previous works.[23,24] Both the highest valence band and the lowest conduction band are almost flat along the ***M*-*Z*-*M′*-*P*-*M*** line of the Brillouin zone and optical transitions for energies close to the bandgap are expected to occur along this line.

The nonresonant Raman spectrum obtained from the density functional perturbation theory (DFPT) calculations is shown in Figure 1(c). According to group theory and the calculated phonon dispersion relation (Figure S2(a)), GaTe has 36 phonon modes in total, 18 of which are Raman-active: 12 A_g modes and 6 B_g modes. The calculated frequency values and vibrational motions of all the 36 phonon modes are listed in Table S1 and Figure S3, respectively. Most of the calculated Raman peaks were also observed in our experiments, as seen in Figure 1(d) for a Raman spectrum on a multilayer GaTe flake measured in vacuum. The Raman modes that were not observed in experiments have either weak intensity or low frequency (<100 cm^{-1}), which is out of the detection range of conventional Raman spectrometers.

DOI: 10.1021/acsnano.6b05002
ACS Nano 2016, 10, 8964−8972

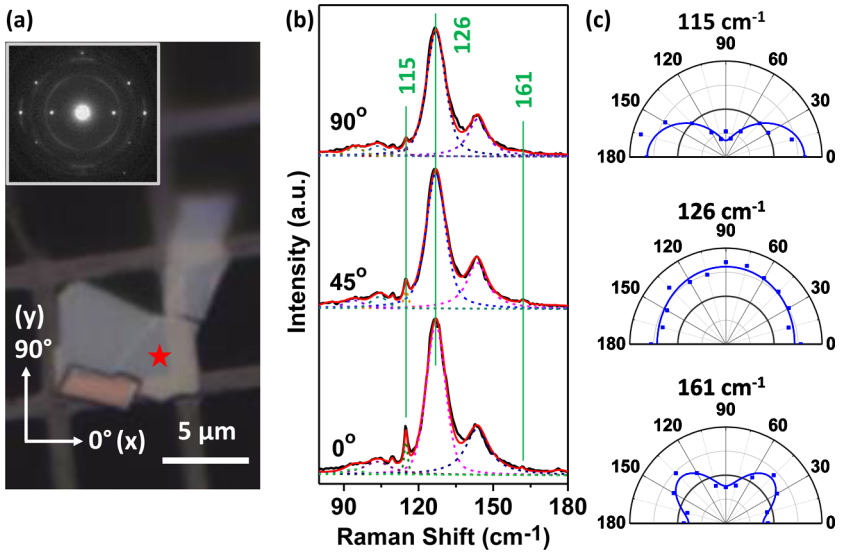

Figure 2. Polarized Raman spectra and diffraction pattern of a GaTe flake on a TEM grid. (a) The optical image of the GaTe flake on the TEM grid. 0° (90°) corresponds to *x*- (*y*-) axis of the GaTe crystal. The star indicates where the measurement was performed. Inset: The corresponding electron diffraction pattern. (b) Polarized Raman spectra of GaTe with polarization angles 0°, 45° and 90°. (c) The Raman intensity *vs* polarization angle for three typical types of Raman modes: A_g mode (115 cm^{-1}), double-resonant mode (126 cm^{-1}) and B_g mode (161 cm^{-1}); these three modes are also marked in (b). The squares are experimental values and the curves are numerical fittings. The Raman shift values are labeled above each panel. The excitation wavelength in (b,c) is 633 nm.

To study the in-plane anisotropic optical properties, we carried out angle-resolved polarized Raman measurements. In Figure 2, the optical image (Figure 2(a)) of a GaTe flake on a TEM (transmission electron microscopy) grid is shown together with the corresponding TEM diffraction pattern (inset of Figure 2(a)) and the polarized Raman spectra (Figure 2(b)) with different polarization angles under parallel configuration. Raman spectra for additional polarization angles and peak fittings are shown in Figure S4. Eight Raman modes can be readily observed experimentally: 107, 115, 126, 142, 161, 208, 268, and 280 cm^{-1}. From the electron diffraction pattern, the 0° axis corresponds to the *x*-axis of the crystalline orientation shown in Figure 1(a-b). According to the DFPT calculations, five Raman modes are A_g modes (107, 115, 208, 268, 280 cm^{-1}), one is B_g mode (161 cm^{-1}), and two are double-resonant modes (126, 142 cm^{-1}). These double-resonant modes[35,36] are created by two phonons of ∼60 cm^{-1} and ∼70 cm^{-1}, respectively, showing their broad features with Raman intensities proportional to the excitation laser power (Figure S2(b)). The shape of the phonon dispersion is flat and the phonon density of states is large around 60−70 cm^{-1}, which is in good agreement with our observation that the Raman modes at 126 and 142 cm^{-1} are strong.[37,38] Moreover, double-resonant modes generally have a weak anisotropy and exhibit broad features because many different combinations for two phonons are possible to contribute to Raman intensity (not necessarily just the Γ point phonons).

The polar plots of the angle-resolved polarized Raman intensity are summarized in Figure 2(c) for three typical Raman modes: A_g (115 cm^{-1}), double-resonant (126 cm^{-1}) and B_g (161 cm^{-1}) modes, which are also marked in Figure 2(b). The polar plots of other modes are shown in Figure S5. It can be seen that Raman-active modes show a variety of degrees of anisotropy: under 633 nm laser excitation, the double-resonant modes at 126 and 142 cm^{-1} exhibit weak anisotropy, while the modes at 107, 115, 208, 268, and 280 cm^{-1} show relatively stronger anisotropy with a period of 180° and with maximum intensities along the *x*-axis.[37] This anisotropy supports the interpretation of the five modes with the same A_g symmetry. On the other hand, the mode around 161 cm^{-1} shows a 4-fold anisotropy with a period of 90°, and the maximum (minimum) intensities along 45° and 135° (along the crystal axes *x* and *y*). This further confirms the different symmetry (B_g) of the 161 cm^{-1} mode[37] compared to the five other modes with A_g symmetry. It can be seen that the crystalline orientation directly probed by TEM (inset of Figure 2(a)) is well matched with the polarized Raman profiles (Figures 2(c) and S5). These phenomena in GaTe show that polarized Raman spectroscopy can indicate crystalline orientation, and the anisotropy of the Raman intensity is strongly related to phonon symmetry. Similar phenomena have also been reported in other 2D materials with in-plane anisotropy.[39,40]

Furthermore, the detailed dependences of the in-plane anisotropy of the Raman intensity on different factors: flake thickness, excitation laser wavelength and phonon frequency, were all studied. In Table 1, we list the polar plots of the polarized Raman intensities under different excitation wavelengths (532, 633, and 785 nm) and with different flake thicknesses (58 and 136 nm) for first-order Raman modes at 107, 115, 161, 208, 268, and 280 cm^{-1}. Table S2 shows the same information for double-resonant modes (126, 142 cm^{-1}). The flakes used for the Raman measurements in Table 1 are mechanically exfoliated from a single-crystal bulk GaTe, and show variations in thicknesses but are physically connected that ensures the same crystalline orientation. In fact, we have measured more than 60 flakes, and found that the Raman profiles are maintained for thicknesses from 51 to 68 nm, in which the 58 nm-thickness is chosen as the representative for this thickness range. Similarly, the Raman profiles for the flake with a thickness of 136 nm also represent the thickness range from 110 to 170 nm. For few-layer flakes (thickness smaller than ∼15 nm), the Raman signals are very weak, partly due to the change of the atomic structure and the small light-matter interactions in those GaTe flakes.[19,20]

DOI: 10.1021/acsnano.6b05002
ACS Nano 2016, 10, 8964−8972

Table 1. Raman Anisotropy Dependence on Flake Thickness, Laser Wavelength and Phonon Frequency[a]

Laser / Peak (cm^{-1})	532 nm		633 nm		785 nm	
	Thin (58 nm)	Thick (136 nm)	Thin	Thick	Thin	Thick
107	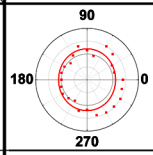	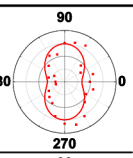	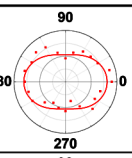	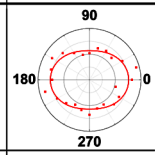	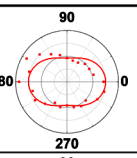	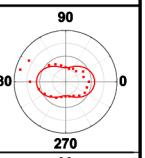
115	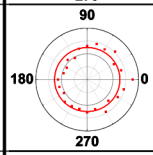	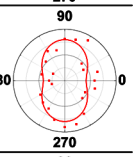	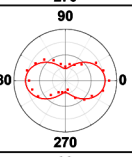	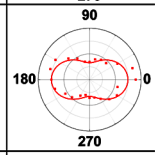	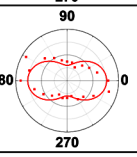	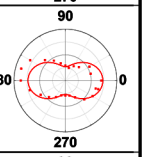
161	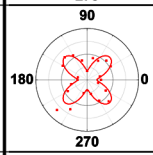	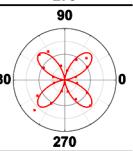	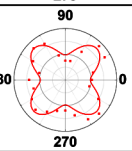	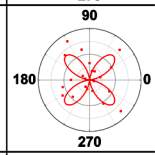	weak	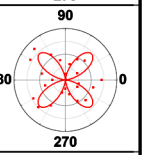
208	weak	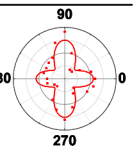	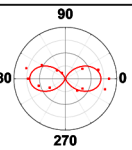	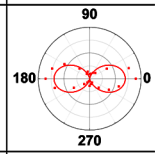	weak	weak
268	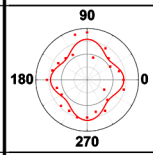	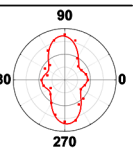	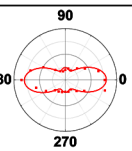	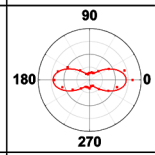	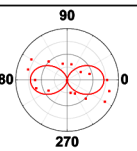	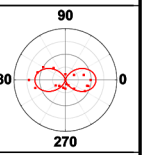
280	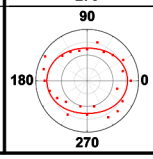		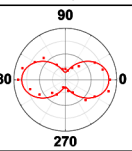	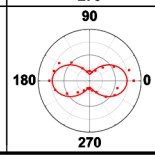	weak	weak

[a]The Raman intensity polar plots of two flakes with typical thicknesses: 58 and 136 nm, are shown here. These two flakes have the same crystalline orientation. The dots are experimental values and the curves are numerical fittings. The laser excitation wavelengths and the Raman frequencies are also labeled. 0° (90°) corresponds to *x*- (*y*-) axis of the GaTe crystal.

As seen in Table 1, the degree of anisotropy for the Raman modes depends not only on phonon mode symmetry, but also on phonon frequency (phonon energy), excitation laser wavelength (photon energy) and flake thickness. It can be seen from Table 1 that the major maximum of the Raman intensity is aligned along either 0° or 90° for all the Raman modes except for the 161 cm^{-1} mode, and for all the excitation wavelengths used. This indicates that either 0° or 90° corresponds to the *x*-axis of the GaTe crystal. The Raman anisotropic profiles are observed to change with laser excitation wavelengths: the major maxima for 532 nm laser excitation are seen to be rotated by 90° from the major maxima for the 633 and 785 nm laser excitation for some Raman modes, such as the 107, 115, 208, and 268 cm^{-1} modes. We also notice that the major maxima of the polarized Raman intensity remain along the same direction (along 0°) for all the A_g modes measured under 633 and 785 nm laser excitations, but can change their directions to be either along 0° or 90° for 532 nm laser. According to the results in Figure 2, the major maxima for the Raman polar plots of the A_g modes with 633 nm laser excitation correspond to the *x*-axis of the crystal. Therefore, in Table 1, 0° corresponds to the *x*-axis of the GaTe crystal. The two groups of flake thicknesses presented here also show differences in the Raman profiles, which indicates the dependence of the anisotropic light-matter interactions on the flake thickness. From Table 1, we can see that the thin and thick flakes share the same major maxima direction (either at 0° or at 90°) for different Raman modes and excitation wavelengths. The Raman anisotropy dependence on flake thickness is reflected in the polar plot shape (or the degree of anisotropy): some modes show stronger anisotropy for the thick flakes than the thin flakes (such as 107, 115, 268, 280 cm^{-1} modes under 532 nm laser), but some show similar degrees of anisotropy for both the thin and the thick flakes (such as 107 cm^{-1} mode under 633 nm laser, and 115 cm^{-1} mode under 785 nm laser), and some show stronger anisotropy for the thin flakes than the thick ones (such as 115 cm^{-1} mode under 633 nm laser). This complexity in the degree of anisotropy can be explained by the optical transition selection rules, which will be described below. In addition, it can be seen that for some modes, secondary maxima appear, such as those at 0° for the 208 and 268 cm^{-1} modes, and at 90° for the 280 cm^{-1} mode measured under 532 nm (E_L = 2.33 eV) laser excitation in the thick flakes. This observation is similar to the case of BP,[15,40,41] and suggests that the light

DOI: 10.1021/acsnano.6b05002
ACS Nano 2016, 10, 8964–8972

absorption, birefringence and phase difference in the Raman tensor elements are relevant for GaTe.[40−42] We can also see that the secondary maxima for the thick flakes are more pronounced than those measured for the thin ones for certain modes (268 and 280 cm^{-1} under 532 nm laser). These observations further confirm that the secondary maxima are related to the optical absorption of GaTe and to the birefringence effect,[15,40−42] since the thicker flakes have larger absorption and the absorption coefficient of GaTe at 2.33 eV (532 nm) is larger than that at 1.96 eV (633 nm) and at 1.58 eV (785 nm). These effects will be explained below. The results presented in Table 1 provide a strong indication of the anisotropic Raman intensity in GaTe and its intricate dependence on phonon energy, photon energy and flake thickness, which offers useful guidelines for the applications of GaTe.

Besides Raman scattering, we further studied the optical absorption and optical extinction of GaTe flakes. The extinction is calculated as $\ln(I_0/I)$, where I and I_0 are the light intensities transmitted through the quartz substrate on and off a GaTe flake, respectively. Since the origin of the extinction is optical absorption in GaTe, it is important to measure the anisotropy of optical extinction. Here we measured the extinction spectra in the wavelength range from 450 to 790 nm. The extinction for nonpolarized light increases with increasing flake thicknesses (Figure S6). For very thin GaTe flakes, such as the 6 nm-thick flake, almost no optical extinction is observed. The extinction of GaTe for polarized light was further investigated for the flakes on a quartz substrate shown in Figure 3(a). In order to determine the crystalline orientation of the flakes, we used the results of polarized Raman measurements on them (Figure S7), which indicated the 0° and 90° orientations in Figure 3(a) correspond to x- and y-axes, respectively.

The optical extinction spectra on the 112 nm-thick flake (labeled with a star in Figure 3(a)) for x- and y-polarized incident light are shown in Figure 3(b). It can be seen that the extinction for y-polarization is slightly smaller than for x-polarization, indicating that the optical extinction in multilayer GaTe shows weak anisotropy, despite the in-plane low symmetry and structural anisotropy of GaTe. The inset in Figure 3(b) shows a polar plot for the extinction of the 112 nm-thick flake at wavelengths of 532 and 633 nm (E_L = 2.33, 1.96 eV, respectively) at different polarization angles, which also indicates the weak in-plane anisotropy of the optical extinction in the GaTe flake. More polarized extinction profiles for the other connected flakes (see Figure 3(a)) are shown in Figure S7(b−f), indicating weak extinction anisotropy, and slightly stronger optical extinction for the x-polarized light than for the y-polarized light as well. Such weak anisotropy in the optical extinction of GaTe is consistent with the previous work on bulk samples.[2] Figure 3(c) shows the thickness dependence of the ratio of the integrated extinctions in the visible range (450 to 790 nm) along the x- and y-directions, which indicates extinction anisotropy. It can be observed that the ratio is small for all the measured thicknesses (below 1.3), suggesting the weak anisotropy of the optical extinction in GaTe. In thin flakes (thickness smaller than ~40 nm), the extinction ratio is relatively large and can reach ~1.3. The ratio drops as thickness increases and becomes close to 1.0 (isotropic) for the thickness range 50−130 nm. For even thicker flakes (>160 nm), there is a rise of the extinction ratio and this rise is probably due to interference effect of light multireflected at the boundaries of

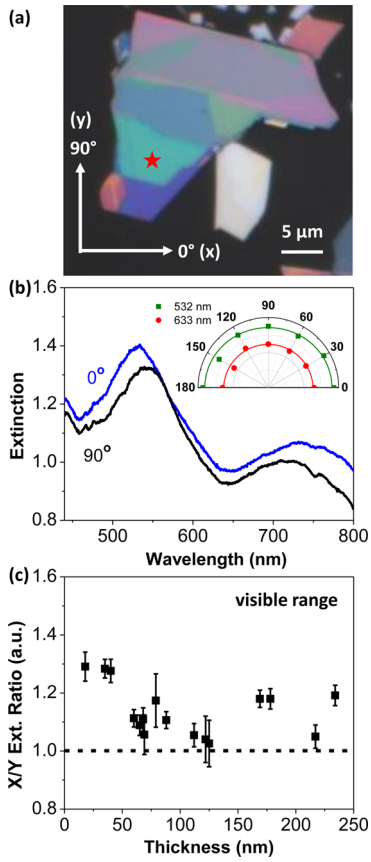

Figure 3. Experimental optical extinction of GaTe. (a) The optical microscope image of GaTe flakes on a quartz substrate. (b) Polarized optical extinction spectra measured with incident light polarized at 0° and 90° on the flake labeled with a star in (a). The flake thickness is 112 nm. The inset of (b) shows the extinction at wavelengths 532 and 633 nm with different polarization angles. The polarization angles correspond to the angular coordinates in (a). From the polarized Raman results shown in Figure S7(g,h), 0° and 90° correspond to x- and y- axes of the GaTe crystal, respectively. (c) Thickness dependence of the extinction ratio of x- and y- polarized light. The optical extinction is integrated in the visible spectral range from 450 to 790 nm. The dashed horizontal line indicates that the ratio equals 1.0 (isotropic).

quartz substrate and GaTe flake, which can play a role when the thickness of the flake is comparable to or larger than the wavelength of light but is negligible for thin flakes. The extinction ratios at the individual wavelengths 532, 633, and 785 nm are provided in Figure S8, which show the similar thickness evolution as in Figure 3(c). Some other anisotropic 2D materials, such as BP,[15,43] show stronger anisotropy in optical extinction than GaTe. The ratio of the integrated extinction of BP in the visible range can be 1.6 for a 225 nm-thick flake and 1.5 for a 9 nm-thick flake.[15] The relatively weak extinction anisotropy of GaTe is advantageous for its practical application in optoelectronic devices, in the sense that the device performance is not sensitive to the polarization angle of the incident light and thus does not require a strict crystalline orientation determination for general use. However, the flake thickness and the choice of substrate should be considered in the design of optoelectronic devices based on GaTe.

In order to explain the observed anisotropies of Raman scattering and optical extinction for GaTe, we carried out a calculation of the electron−photon interactions. The details of

DOI: 10.1021/acsnano.6b05002
ACS Nano 2016, 10, 8964−8972

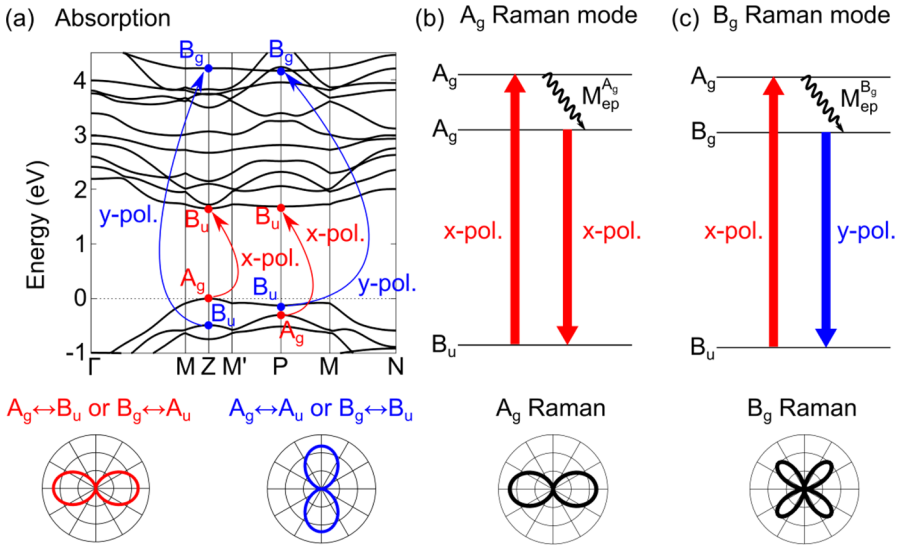

Figure 4. Optical transition selection rules in bulk GaTe. (a) Selection rules of optical transition near the Fermi energy at the *P* and *Z* points in the Brillouin zone, and the anisotropic optical absorption corresponding to the transitions activated by *x*-polarized (red arrows and curve) and *y*-polarized (blue arrows and curve) light. (b,c) One of the expected transitions for Raman scattering and polarization shape for the A_g (b) and B_g (c) modes at the *Z* or *P* point. $M_{ep}^{A_g}$ ($M_{ep}^{B_g}$) indicates the electron−phonon interaction emitting an A_g (B_g) phonon. Red and blue arrows indicate the transition activated by *x*- and *y*-polarized light, respectively. In (a−c), the horizontal (vertical) axes in the polar plots correspond to *x*- (*y*-) axes.

the calculation can be found in Section 1 of Supporting Information (SI). Briefly, the optical absorption spectra can be obtained by calculating absorption coefficient α. According to Fermi's Golden Rule, α is proportional to the square of the electron−photon matrix element, $\langle m|H_{op}|i\rangle$,[44] which describes the optical transition from the state i to m, and the matrix element is given by the inner product of the dipole vector $\langle m|\nabla|i\rangle$ and the light polarization vector. When the polarization of the incident light changes, this inner product gives the polarization dependence of α. On the other hand, when the state m or i changes by changing the flake thickness or the laser excitation wavelength, the matrix element $\langle m|H_{op}|i\rangle$ and its polarization dependence change correspondingly. This result is known as the optical transition selection rules, and can be explained by group theory (details in Section 2 of SI). In the case of monoclinic bulk GaTe, the high symmetry points ***Γ***, ***Z*** and ***P*** in the Brillouin zone belong to the C_{2h}^3 ($C2/m$) space group. The symmetry of the eigenfunction for each energy band at the ***Z*** and ***P*** points (Figure S9) was determined by first-principles calculation. The ***Z*** and ***P*** points have the largest probability for optical transitions, and Figure 4(a) shows the selection rules of the optical transitions near the Fermi energy. The transitions between the A_g state and the B_u state and between the A_u state and the B_g state occur by *x*-polarized light, while the transitions between the A_g state and the A_u state and between the B_g state and the B_u state occur by *y*-polarized light. The main contribution near the gap energy (λ > 600 nm) comes from *x*-polarized light, and as the photon energy increases, the *y*-polarized light is partially absorbed and the optical absorption/extinction anisotropy becomes weaker. This is due to the involvement of more energy bands in the absorption which contribute to different anisotropies as the photon energy increases. In line with the experimental results, the calculation also yields larger absorption for *x*- than for *y*-polarized light for the photon energy near the bandgap (Figure S10(a)).

With these selection rules of optical transitions and group theory, we can explain the intricate Raman polarization dependence presented in Table 1. The Raman intensity can be obtained by incorporating two electron−photon matrix elements with one electron−phonon matrix element as follows:

$$I_\nu(E_L) = \left| \sum_{i,m,m'} \frac{\langle f|H_{op}|m'\rangle\langle m'|H_{ep}^{\nu}|m\rangle\langle m|H_{op}|i\rangle}{(E_L - \Delta E_{mi})(E_L - \hbar\omega_\nu - \Delta E_{m'i})} \right|^2 \quad (1)$$

where $\Delta E_{mi} = E_m - E_i - i\Gamma$, m (m') is the intermediate state and Γ is a broadening factor corresponding to the lifetime of photoexcited electrons. The initial (i) and final (f) states are the same in a Raman process. If we neglect the polarization dependence of the electron−phonon matrix element $\langle m'|H_{ep}^{\nu}|m\rangle$, the polarization dependence of the Raman intensity can be described by the product of two electron−photon matrix elements, $\langle f|H_{op}|m'\rangle$ and $\langle m|H_{op}|i\rangle$. We show the detailed selection rules for the A_g and B_g Raman modes in Section 3 of SI, and an example of the transition corresponding to the A_g and B_g modes at the ***Z*** or ***P*** point in Figure 4(b,c). For the A_g mode, the m and m' states have the same symmetry, and the two electron−photon interaction matrix elements in eq 1 have the same polarization dependence that gives a 180° period in the polarization dependence; while for the B_g mode, the m and m' states have different symmetries, and the two matrix elements have the opposite polarization dependences, resulting in the 90° period of the B_g polarization profile, which is consistent with the experimental results shown in Table 1. Using the above analyses, we can explain the phenomena of major maximum axis flipping shown in Table 1: for Raman modes under 532 nm laser excitation, the major axis can flip between 0° and 90°, while 633 and 785 nm lasers do not induce such flipping of major axes. This is because 532 nm (2.33 eV) laser can excite the electrons to several energy bands with different symmetries, making a complicated polarization profile. Moreover, at low laser excitation energy, the Raman

DOI: 10.1021/acsnano.6b05002
ACS Nano 2016, 10, 8964−8972

modes are mostly x-polarized, while at higher laser excitation energy, the Raman modes polarized along the y-axis exist (Figure 4(a)), which is in a good agreement with the experimental observations in Table 1. The differences in the degree of anisotropy for different flake thicknesses (Table 1) are due to the change in the energy band structures with flake thickness. Besides, it is observed in Table 1 that under 532 nm laser, the 280 cm^{-1} Raman mode has x-polarization, different from the other A_g modes with y-polarization. This is because the electronic states involved in the Raman process are related to the phonon energy. Therefore, it is possible that under 532 nm laser and for the 280 cm^{-1} phonon, x-polarized electron−photon interactions dominate, while for the other A_g modes with different phonon energies, the electron−photon interactions with y-polarization are dominant.

Our optical transition selection rules using quantum mechanical model and group theory are essential for the analysis of the Raman anisotropy in GaTe. If we adopt the classical theory of the Raman tensor for the polarization dependence of the Raman intensity, the phonon modes with the same symmetry would have the same polarization dependence under the same excitation wavelength.[45] However, as can be observed from Table 1, under 532 nm laser excitation, the maximum intensity for the A_g mode at 280 cm^{-1} is along the y-axis, while the other A_g modes at 107, 115, 208, 268 cm^{-1} are polarized toward the x-axis, which suggests the necessity of using quantum theory for the Raman intensity (eq 1) for understanding the polarization dependence.[45] Since we notice that there is small discrepancy of anisotropy between theory and experiment, it is expected that the anisotropy of the electron−phonon interaction contributes to the anisotropy of the Raman intensity, which will be part of the future work. This method of characterizing the optical anisotropy of GaTe can be generalized to other 2D materials with in-plane anisotropy, which should be of significant importance for designing thermoelectric, electronic and photonic devices.

In addition, it is demonstrated through calculation (see Section 4 of SI for details) that the interference effect can affect the anisotropies in the optical absorption and extinction, but is not as important for the Raman anisotropy (Figures S11−S12).[40,46−48] For the optical absorption, the calculation involving the interference effect (Figure S11(b,c)) reduces the intrinsic absorption anisotropy, which is obtained solely by the electron−photon matrix elements. It suggests that the interference effect plays an important role in the optical absorption and extinction in GaTe, which is consistent with the experimental results. However, the experimentally observed anisotropy of the Raman intensity cannot be mainly attributed to the interference effect (Figure S12(b)), but is mostly due to the anisotropy of light-matter interactions.

On the basis of the theory we developed, it is expected that intricate in-plane anisotropy occurs in many low-symmetry 2D materials. Indeed, it has been reported that Raman spectroscopy shows polarization dependence on the crystalline orientation for various low-symmetry 2D materials, such as in BP, GaTe, $ReSe_2$, ReS_2, SnSe, *etc.*[45] The dependence is related to the symmetry of the material. For example, the major axis of Raman intensity polar plot is along either the zigzag or armchair directions for the A_g modes in BP with D_{2h} symmetry, while in $ReSe_2$ and ReS_2 which have $P\bar{1}$ symmetry, the major axis can be along different lattice directions.[49,50] Furthermore, due to the complexity of Raman process, such a polarization dependence can vary with factors such as excitation laser wavelength, flake thickness, phonon frequency, *etc.*[15,41] The anisotropy of optical absorption and extinction can also be observed in some anisotropic 2D materials, but the degree of anisotropy depends on the actual electronic energy bands of the material and may not be directly connected to the structural anisotropy of the material. For example, BP with higher structural symmetry D_{2h}, shows stronger anisotropy of the optical absorption in the visible range than GaTe, which has relatively lower structural symmetry C_{2h}.[15] By the same token, the mobility anisotropy may not be directly related to the structural anisotropy, but is more closely related to the energy band diagram.[12] More studies on the anisotropic optical and electronic properties of other in-plane anisotropic 2D materials are necessary for the future applications of such materials, to provide more guidance on particular choices of materials to use for particular applications.

CONCLUSION

In summary, we performed an experiment/theory integrated investigation of the anisotropic optical extinction and Raman scattering in GaTe, which reveals insights into the role of anisotropy in light-matter interactions. The anisotropy of optical extinction is generally weak in the visible spectral range for multilayer GaTe, despite the in-plane structural anisotropy for GaTe. However, the anisotropy of the Raman intensity is strong and sensitively depends on excitation laser energy, phonon energy and GaTe thickness. This intricate dependence of the Raman scattering anisotropy on these different parameters stems from optical transition selection rules, as dictated by group theory. This work underscores the importance of understanding the anisotropic light-matter interactions in GaTe as well as other layered materials with low symmetry and in-plane anisotropy. This work also provides useful guidelines for the exploration of applications in electronic, optoelectronic and thermoelectric devices based on GaTe.

METHODS

Sample Preparation and Characterization. GaTe flakes were mechanically exfoliated from a bulk single-crystal GaTe onto 300 nm SiO_2/Si or quartz substrates. The thicknesses of the flakes were measured by atomic force microscopy (AFM). To transfer the GaTe flakes onto the TEM grid, we first exfoliated the GaTe flakes onto a PMMA thin film spin-coated on a Si substrate. The locations of the GaTe flakes were identified using an optical microscope, and a C-flat TEM grid was placed upside-down on the GaTe flake. Then the TEM grid was sealed in a drop of PMMA to fix the position, and the whole structure was immersed in acetone to remove PMMA, ending up with GaTe flakes lying flat and clean on the TEM grid. The TEM measurement was made using the facility of Joel 2011 TEM. The selected area electron diffraction (SAED) pattern of the sample as shown in the inset of Figure 2(a) was taken with a camera length of 15 cm.

Raman Measurements. Raman spectra were measured using a Horiba Jobin-Yvon HR800 system with three excitation lasers (532, 633, and 785 nm). A 100× objective was used to focus the laser beam on the sample with the spot size of approximately 1 μm. The laser power at the sample location was about 0.5 mW. In the polarization dependence measurements, parallel backscattering configuration was used with the capability of sample rotation. The Raman peak parameters were obtained by fitting the spectra with Lorentzian/Gaussian line shapes.

Microextinction Measurements. The extinction spectra were measured on GaTe flakes placed on 0.5 mm thick quartz substrates using a home-built microextinction setup operating in the transmission

DOI: 10.1021/acsnano.6b05002
ACS Nano 2016, 10, 8964−8972

mode. The white light source (EQ-99XFC, Energetiq) was coupled out with 25 μm diameter optical fiber. The white light was focused on the sample surface with spot size ~1.5 μm using two microscope objectives: a 5×-collimating objective, NA (numeric aperture) = 0.1, and a 100×-long working distance objective, NA = 0.8 in an inverted microscope. The transmitted light was collected by a 50×-objective (NA = 0.5) in an upright microscope coupled to the inverted microscope, and was analyzed by a spectrometer (Spectra Pro 2300i, f = 0.3 m) equipped with a CCD camera (Pixis 256BR, Princeton Instruments). The extinction was calculated as $\ln(I_0/I)$, where I and I_0 are the light intensities transmitted through the quartz substrate on and off a GaTe flake, respectively. Here the extinction includes both optical absorption and reflection which is analyzed theoretically in SI. For the polarized microextinction measurements, the incident white light was linearly polarized using a Glan-Taylor polarizer.

Theoretical Calculations. The electronic band structure of GaTe was calculated within the DFT method as implemented in the Quantum Espresso package.[51] We used a generalized gradient approximation (GGA) with Perdew–Burke–Ernzerhof (PBE) functional. Norm-conserving pseudopotential was used.[52] The kinetic energy cutoff for wave functions was set at 50 Ry. The Monkhorst–Pack scheme with 8 × 8 × 8 mesh was used to sample k-points of the Brillouin zone of bulk GaTe. Atomic coordinates of bulk GaTe were determined from experimental results.[53,54] The phonon dispersion relation of GaTe was calculated based on density functional perturbation theory[55] and the nonresonant Raman intensities were calculated based on Placzek approximation as introduced by Lazzeri and Mauri.[56]

ASSOCIATED CONTENT

Supporting Information

The Supporting Information is available free of charge on the ACS Publications website at DOI: 10.1021/acsnano.6b05002.

Detailed calculation of electron–photon interactions, theory of optical transition selection rules and group theory, detailed calculation of interference effect, calculated energy band diagrams and phonon dispersion relation, more spectra and polar plots of experimental Raman scattering and optical extinction, all phonon modes of GaTe from DFPT calculation (PDF)

AUTHOR INFORMATION

Corresponding Authors

*E-mail: xiling@mit.edu.
*E-mail: millie@mgm.mit.edu.

Author Contributions

S.H., X.L., J.K. and M.S.D. initiated the project and designed the experiments. S.H., X.L., G.W. and A.A.P. performed experimental measurements and analyzed the data. Y.T., H.G., T.Y. and R.S. performed the theoretical analysis. Z.W. and J.L. helped with TEM measurements.

Notes

The authors declare no competing financial interest.

ACKNOWLEDGMENTS

S.H., X.L. and M.S.D. at MIT acknowledge National Science Foundation grant 2DARE (EFRI-1542815) for financial support. J.K. acknowledges support from U.S. Army Research Office through the MIT Institute for Soldier Nanotechnologies, under award number 023674. Microextinction measurements were conducted at the Center for Nanophase Materials Sciences, which is a DOE Office of Science User Facility. R.S. acknowledges MEXT grant (No. 25107005). T.Y. and H.G. acknowledge the NSFC Grant (No. 51331006, U1537204) and Liaoning Shihua University Grant (2016XJJ-044) for financial support. T.Y. acknowledges China Scholarship Council for financial support.

REFERENCES

(1) Ling, X.; Wang, H.; Huang, S.; Xia, F.; Dresselhaus, M. S. The Renaissance of Black Phosphorus. *Proc. Natl. Acad. Sci. U. S. A.* **2015**, *112*, 201416581.

(2) Sánchez-Royo, J. F.; Segura, A.; Muñoz, V. Anisotropy of the refractive index and absorption coefficient in the layer plane of gallium telluride single crystals. *Phys. Status Solidi* **1995**, *151*, 257–265.

(3) Lucovsky, G.; White, R. M. Optical-Phonon Anisotropies in Layered Crystals. *Nuovo Cim. B Ser. 11* **1977**, *38*, 290–300.

(4) Taube, A.; Łapińska, A.; Judek, J.; Zdrojek, M. Temperature Dependence of Raman Shifts in Layered ReSe2 and SnSe2 Semiconductor Nanosheets. *Appl. Phys. Lett.* **2015**, *107*, 013105.

(5) Chenet, D. A.; Aslan, O. B.; Huang, P. Y.; Fan, C.; van der Zande, A. M.; Heinz, T. F.; Hone, J. C. In-Plane Anisotropy in Mono- and Few-Layer ReS2 Probed by Raman Spectroscopy and Scanning Transmission Electron Microscopy. *Nano Lett.* **2015**, *15*, 5667–5672.

(6) Wang, H.; Wang, X.; Xia, F.; Wang, L.; Jiang, H.; Xia, Q.; Chin, M. L.; Dubey, M.; Han, S. Black Phosphorus Radio-Frequency Transistors. *Nano Lett.* **2014**, *14*, 6424–6429.

(7) Low, T.; Rodin, A. S.; Carvalho, A.; Jiang, Y.; Wang, H.; Xia, F.; Castro Neto, A. H. Tunable Optical Properties of Multilayer Black Phosphorus Thin Films. *Phys. Rev. B: Condens. Matter Mater. Phys.* **2014**, *90*, 075434.

(8) Wang, X.; Jones, A. M.; Seyler, K. L.; Tran, V.; Jia, Y.; Zhao, H.; Wang, H.; Yang, L.; Xu, X.; Xia, F. Highly Anisotropic and Robust Excitons in Monolayer Black Phosphorus. *Nat. Nanotechnol.* **2015**, *10*, 517–521.

(9) Ho, C. H.; Huang, Y. S.; Tiong, K. K.; Liao, P. C. Absorption-Edge Anisotropy in ReS 2 and ReSe 2 Layered Semiconductors. *Phys. Rev. B: Condens. Matter Mater. Phys.* **1998**, *58*, 16130–16135.

(10) Ho, C. H.; Huang, Y. S.; Tiong, K. K. In-Plane Anisotropy of the Optical and Electrical Properties of ReS2 and ReSe2 Layered Crystals. *J. Alloys Compd.* **2001**, *317–318*, 222–226.

(11) Guo, R.; Wang, X.; Kuang, Y.; Huang, B. First-Principles Study of Anisotropic Thermoelectric Transport Properties of IV-VI Semiconductor Compounds SnSe and SnS. *Phys. Rev. B: Condens. Matter Mater. Phys.* **2015**, *92*, 115202.

(12) Xia, F.; Wang, H.; Jia, Y. Rediscovering Black Phosphorus as an Anisotropic Layered Material for Optoelectronics and Electronics. *Nat. Commun.* **2014**, *5*, 4458.

(13) Luo, Z.; Maassen, J.; Deng, Y.; Du, Y.; Garrelts, R. P.; Lundstrom, M. S.; Ye, P. D.; Xu, X. Anisotropic in-Plane Thermal Conductivity Observed in Few-Layer Black Phosphorus. *Nat. Commun.* **2015**, *6*, 8572.

(14) Lee, S.; Yang, F.; Suh, J.; Yang, S.; Lee, Y.; Li, G.; Sung Choe, H.; Suslu, A.; Chen, Y.; Ko, C.; Park, J.; Liu, K.; Li, J.; Hippalgaonkar, K.; Urban, J. J.; Tongay, S.; Wu, J. Anisotropic in-Plane Thermal Conductivity of Black Phosphorus Nanoribbons at Temperatures Higher than 100 K. *Nat. Commun.* **2015**, *6*, 8573.

(15) Ling, X.; Huang, S.; Hasdeo, E. H.; Liang, L.; Parkin, W. M.; Tatsumi, Y.; Nugraha, A. R. T.; Puretzky, A. A.; Das, P. M.; Sumpter, B. G.; Geohegan, D. B.; Kong, J.; Saito, R.; Drndic, M.; Meunier, V.; Dresselhaus, M. S. Anisotropic Electron-Photon and Electron-Phonon Interactions in Black Phosphorus. *Nano Lett.* **2016**, *16*, 2260–2267.

(16) Xia, F.; Wang, H.; Xiao, D.; Dubey, M.; Ramasubramaniam, A. Two-Dimensional Material Nanophotonics. *Nat. Photonics* **2014**, *8*, 899–907.

(17) Liu, E.; Fu, Y.; Wang, Y.; Feng, Y.; Liu, H.; Wan, X.; Zhou, W.; Wang, B.; Shao, L.; Ho, C.-H.; Huang, Y.-S.; Cao, Z.; Wang, L.; Li, A.; Zeng, J.; Song, F.; Wang, X.; Shi, Y.; Yuan, H.; Hwang, H. Y.; et al. Integrated Digital Inverters Based on Two-Dimensional Anisotropic ReS2 Field-Effect Transistors. *Nat. Commun.* **2015**, *6*, 6991.

(18) Zólyomi, V.; Drummond, N. D.; Fal'ko, V. I. Band Structure and Optical Transitions in Atomic Layers of Hexagonal Gallium

DOI: 10.1021/acsnano.6b05002
ACS Nano 2016, 10, 8964–8972

Chalcogenides. *Phys. Rev. B: Condens. Matter Mater. Phys.* **2013**, *87*, 195403.
(19) Hu, P.; Zhang, J.; Yoon, M.; Qiao, X.-F.; Zhang, X.; Feng, W.; Tan, P.; Zheng, W.; Liu, J.; Wang, X.; Idrobo, J. C.; Geohegan, D. B.; Xiao, K. Highly Sensitive Phototransistors Based on Two-Dimensional GaTe Nanosheets with Direct Bandgap. *Nano Res.* **2014**, *7*, 694−703.
(20) Liu, F.; Shimotani, H.; Shang, H.; Kanagasekaran, T.; Zólyomi, V.; Drummond, N.; Fal'ko, V. I.; Tanigaki, K. High-Sensitivity Photodetectors Based on Multilayer GaTe Flakes. *ACS Nano* **2014**, *8*, 752−760.
(21) Balitskii, O. A.; Jaeckel, B.; Jaegermann, W. Surface Properties of GaTe Single Crystals. *Phys. Lett. A* **2008**, *372*, 3303−3306.
(22) Bose, D. N.; Pal, S. Photoconductivity, Low-Temperature Conductivity, and Magnetoresistance Studies on the Layered Semiconductor GaTe. *Phys. Rev. B: Condens. Matter Mater. Phys.* **2001**, *63*, 235321.
(23) Sánchez-Royo, J. F.; Pellicer-Porres, J.; Segura, A.; Muñoz-Sanjosé, V.; Tobías, G.; Ordejón, P.; Canadell, E.; Huttel, Y. Angle-Resolved Photoemission Study and First-Principles Calculation of the Electronic Structure of GaTe. *Phys. Rev. B: Condens. Matter Mater. Phys.* **2002**, *65*, 115201.
(24) Yamamoto, A.; Syouji, A.; Goto, T.; Kulatov, E.; Ohno, K.; Kawazoe, Y.; Uchida, K.; Miura, N. Excitons and Band Structure of Highly Anisotropic GaTe Single Crystals. *Phys. Rev. B: Condens. Matter Mater. Phys.* **2001**, *64*, 035210.
(25) Fonseca, J. J.; Tongay, S.; Topsakal, M.; Chew, A. R.; Lin, A. J.; Ko, C.; Luce, A. V.; Salleo, A.; Wu, J.; Dubon, O. D. Bandgap Restructuring of the Layered Semiconductor Gallium Telluride in Air. *Adv. Mater.* **2016**, *28*, 6465.
(26) Shenoy, U. S.; Gupta, U.; Narang, D. S.; Late, D. J.; Waghmare, U. V.; Rao, C. N. R. Electronic Structure and Properties of Layered Gallium Telluride. *Chem. Phys. Lett.* **2016**, *651*, 148−154.
(27) Susoma, J.; Karvonen, L.; Säynätjoki, A.; Mehravar, S.; Norwood, R. A.; Peyghambarian, N.; Kieu, K.; Lipsanen, H.; Riikonen, J. Second and Third Harmonic Generation in Few-Layer Gallium Telluride Characterized by Multiphoton Microscopy. *Appl. Phys. Lett.* **2016**, *108*, 073103.
(28) Zhao, Q.; Wang, T.; Miao, Y.; Ma, F.; Xie, Y.; Ma, X.; Gu, Y.; Li, J.; He, J.; Chen, B.; Xi, S.; Xu, L.; Zhen, H.; Yin, Z.; Li, J.; Ren, J.; Jie, W. Thickness-Induced Structural Phase Transformation of Layered Gallium Telluride. *Phys. Chem. Chem. Phys.* **2016**, *18*, 18719−18726.
(29) Mandal, K. C.; Krishna, R. M.; Hayes, T. C.; Muzykov, P. G.; Das, S.; Sudarshan, T. S. Layered GaTe Crystals for Radiation Detectors. In *IEEE Nuclear Science Symposuim & Medical Imaging Conference*; IEEE, 2010; pp 3719−3724.
(30) Rahmlow, T. D.; DePoy, D. M.; Fourspring, P. M.; Ehsani, H.; Lazo-Wasem, J. E.; Gratrix, E. J. Development of Front Surface, Spectral Control Filters with Greater Temperature Stability for Thermophotovoltaic Energy Conversion. In *AIP Conference Proceedings*; AIP, 2007; Vol. *890*, pp 59−67.
(31) Pal, S.; Bose, D. Growth, Characterisation and Electrical Anisotropy in Layered Chalcogenides GaTe and InTe. *Solid State Commun.* **1996**, *97*, 725−729.
(32) Gouskov, L.; Gouskov, A. Resistivity Anisotropy in the Layer Plane of GaTe. *Phys. Status Solidi* **1979**, *51*, K213−K215.
(33) Pearson, W. B. The Crystal Structures of Semiconductors and a General Valence Rule. *Acta Crystallogr.* **1964**, *17*, 1−15.
(34) Camassel, J.; Merle, P.; Mathieu, H. Excitonic Absorption Edge of GaTe. *Physica B+C* **1980**, *99*, 309−313.
(35) Guo, H.; Yang, T.; Yamamoto, M.; Zhou, L.; Ishikawa, R.; Ueno, K.; Tsukagoshi, K.; Zhang, Z.; Dresselhaus, M. S.; Saito, R. Double Resonance Raman Modes in Monolayer and Few-Layer MoTe2. *Phys. Rev. B: Condens. Matter Mater. Phys.* **2015**, *91*, 205415.
(36) Venezuela, P.; Lazzeri, M.; Mauri, F. Theory of Double-Resonant Raman Spectra in Graphene: Intensity and Line Shape of Defect-Induced and Two-Phonon Bands. *Phys. Rev. B: Condens. Matter Mater. Phys.* **2011**, *84*, 035433.
(37) Irwin, J. C.; Clayman, B. P.; Mead, D. G. Long-Wavelength Phonons in GaTe. *Phys. Rev. B: Condens. Matter Mater. Phys.* **1979**, *19*, 2099−2105.
(38) Cerdeira, F.; Meneses, E. A.; Gouskov, A. Splittings and Correlations between the Long-Wavelength Optical Phonons in the Layer Compounds GaSe, GaTe, and $GaSe_{1-x}Te_x$. *Phys. Rev. B* **1977**, *16*, 1648−1654.
(39) Wu, J.; Mao, N.; Xie, L.; Xu, H.; Zhang, J. Identifying the Crystalline Orientation of Black Phosphorus Using Angle-Resolved Polarized Raman Spectroscopy. *Angew. Chem.* **2015**, *127*, 2396−2399.
(40) Mao, N.; Wu, J.; Han, B.; Lin, J.; Tong, L.; Zhang, J. Birefringence-Directed Raman Selection Rules in 2D Black Phosphorus Crystals. *Small* **2016**, *12*, 2627−2633.
(41) Ribeiro, H. B.; Pimenta, M. A.; de Matos, C. J. S.; Moreira, R. L.; Rodin, A. S.; Zapata, J. D.; de Souza, E. A. T.; Castro Neto, A. H. Unusual Angular Dependence of the Raman Response in Black Phosphorus. *ACS Nano* **2015**, *9*, 4270−4276.
(42) Kranert, C.; Sturm, C.; Schmidt-Grund, R.; Grundmann, M. Raman Tensor Formalism for Optically Anisotropic Crystals. *Phys. Rev. Lett.* **2016**, *116*, 127401.
(43) Qiao, J.; Kong, X.; Hu, Z.-X.; Yang, F.; Ji, W. High-Mobility Transport Anisotropy and Linear Dichroism in Few-Layer Black Phosphorus. *Nat. Commun.* **2014**, *5*, 4475.
(44) Sakurai, J. J.; Napolitano, J. J. *Modern Quantum Mechanics*, 2nd ed.; Addison-Wesley, 2011.
(45) Saito, R.; Tatsumi, Y.; Huang, S.; Ling, X.; Dresselhaus, M. S. Raman Spectroscopy of Transition Metal Dichalcogenides. *J. Phys.: Condens. Matter* **2016**, *28*, 353002.
(46) Li, S.-L.; Miyazaki, H.; Song, H.; Kuramochi, H.; Nakaharai, S.; Tsukagoshi, K. Quantitative Raman Spectrum and Reliable Thickness Identification for Atomic Layers on Insulating Substrates. *ACS Nano* **2012**, *6*, 7381−7388.
(47) Yoon, D.; Moon, H.; Son, Y.-W.; Choi, J. S.; Park, B. H.; Cha, Y. H.; Kim, Y. D.; Cheong, H. Interference Effect on Raman Spectrum of Graphene on SiO2/Si. *Phys. Rev. B: Condens. Matter Mater. Phys.* **2009**, *80*, 125422.
(48) Wang, Y. Y.; Ni, Z. H.; Shen, Z. X.; Wang, H. M.; Wu, Y. H. Interference Enhancement of Raman Signal of Graphene. *Appl. Phys. Lett.* **2008**, *92*, 043121.
(49) Zhao, H.; Wu, J.; Zhong, H.; Guo, Q.; Wang, X.; Xia, F.; Yang, L.; Tan, P.; Wang, H. Interlayer Interactions in Anisotropic Atomically Thin Rhenium Diselenide. *Nano Res.* **2015**, *8*, 3651−3661.
(50) He, R.; Yan, J.-A.; Yin, Z.; Ye, Z.; Ye, G.; Cheng, J.; Li, J.; Lui, C. H. Coupling and Stacking Order of ReS2 Atomic Layers Revealed by Ultralow-Frequency Raman Spectroscopy. *Nano Lett.* **2016**, *16*, 1404.
(51) Giannozzi, P.; Baroni, S.; Bonini, N.; Calandra, M.; Car, R.; Cavazzoni, C.; Ceresoli, D.; Chiarotti, G. L.; Cococcioni, M.; Dabo, I.; Dal Corso, A.; de Gironcoli, S.; Fabris, S.; Fratesi, G.; Gebauer, R.; Gerstmann, U.; Gougoussis, C.; Kokalj, A.; Lazzeri, M.; Martin-Samos, L.; et al. QUANTUM ESPRESSO: A Modular and Open-Source Software Project for Quantum Simulations of Materials. *J. Phys.: Condens. Matter* **2009**, *21*, 395502.
(52) Hartwigsen, C.; Goedecker, S.; Hutter, J. Relativistic Separable Dual-Space Gaussian Pseudopotentials from H to Rn. *Phys. Rev. B: Condens. Matter Mater. Phys.* **1998**, *58*, 3641−3662.
(53) Alapini, F.; Flahaut, J.; Guittard, M.; Jaulmes, S.; Julien-Pouzol, M. Systeme Gallium-Tellure. *J. Solid State Chem.* **1979**, *28*, 309−319.
(54) HU, S.-Z.; PARTHÉ, E. Inorganic Crystal Structure Data to Be Presented in a Form More Useful for Further Studies. *Chin. J. Struct. Chem.* **2004**, *23*, 1150.
(55) Baroni, S.; de Gironcoli, S.; Dal Corso, A. Phonons and Related Crystal Properties from Density-Functional Perturbation Theory. *Rev. Mod. Phys.* **2001**, *73*, 515−562.
(56) Lazzeri, M.; Mauri, F. First-Principles Calculation of Vibrational Raman Spectra in Large Systems: Signature of Small Rings in Crystalline SiO_2. *Phys. Rev. Lett.* **2003**, *90*, 036401.

DOI: 10.1021/acsnano.6b05002
ACS Nano 2016, 10, 8964−8972

Supporting Information

In-Plane Optical Anisotropy of Layered Gallium Telluride

Shengxi Huang[1], Yuki Tatsumi[2], Xi Ling[1], Huaihong Guo[3], Ziqiang Wang[4], Garrett Watson[5], Alexander A. Puretzky[6], David B. Geohegan[6], Jing Kong[1], Ju Li[4], Teng Yang[2,7], Riichiro Saito[2], Mildred S. Dresselhaus[1,5*]*

[1] Department of Electrical Engineering and Computer Science, Massachusetts Institute of Technology, Cambridge, Massachusetts 02139, USA.

[2] Department of Physics, Tohoku University, Sendai, 980-8578, Japan.

[3] College of sciences, Liaoning Shihua University, Fushun, 113001, China

[4] Department of Nuclear Science and Engineering, Massachusetts Institute of Technology, Cambridge, Massachusetts 02139, USA.

[5] Department of Physics, Massachusetts Institute of Technology, Cambridge, Massachusetts 02139, USA.

[6] Center for Nanophase Materials Sciences, Oak Ridge National Laboratory, Oak Ridge, Tennessee 37831, USA.

[7] Shenyang National Laboratory for Materials Science, Institute of Metal Research, Chinese Academy of Sciences, Shenyang, 110016, China.

*** Corresponding Authors:**

Prof. Mildred S. Dresselhaus

Department of Electrical Engineering and Computer Science,

Massachusetts Institute of Technology, Cambridge, Massachusetts 02139, USA

Tel: +1-617-253-6864

Email: millie@mgm.mit.edu

Dr. Xi Ling

Department of Electrical Engineering and Computer Science,

Massachusetts Institute of Technology, Cambridge, Massachusetts 02139, USA

Tel: +1-617-253-6860

Email: xiling@mit.edu

1. Calculation of optical absorption

In order to explain the observed anisotropy of Raman scattering and optical extinction for GaTe, we carried out a calculation of the electron-photon interaction. The electron-photon matrix element, $\langle m|H_{\mathrm{op}}|i\rangle$, which can be calculated within the dipole approximation,[1] is responsible for an optical transition from the state i to m and is given by

$$\langle m|H_{\mathrm{op}}|i\rangle \propto P \cdot D_{mi} \qquad \text{(S1)}$$

where P is the polarization vector for the incident light, and D_{mi} is the dipole vector defined as $D_{mi} = \langle m|\nabla|i\rangle$. The electronic wave functions for the states i and m are obtained from first-principles density functional theory (DFT) calculations.

Optical extinction and absorption probability can be given by the absorption coefficient α, which is given by the Fermi's Golden Rule:

$$\alpha(E_L) \propto \sum_{m,i} |\langle m|H_{\mathrm{op}}|i\rangle|^2 \delta(E_m - E_i - E_L) \qquad \text{(S2)}$$

where E_L is the energy of the incident photon, and E_i (E_m) is the energy of the electronic state i (m). In the numerical calculations, we approximate the delta function $\delta(E_m - E_i - E_L)$ with a Gaussian function $\frac{1}{\sqrt{2\pi}\gamma} \exp\left\{\frac{(E_m - E_i - E_L)}{2\gamma^2}\right\}$, where γ is a broadening factor corresponding to the lifetime of a photo-excited electron. Here γ can be determined from the spectral width of the optical absorption[2] and we adopt $\gamma = 0.03$ eV in this calculation. The calculated optical absorption spectrum is shown in Figure S10(a). The absorption spectrum thus obtained reproduces the fact that ***x***- (0°) polarized light is more absorbed than ***y***- (90°) polarized light.

2. Analysis of the absorption anisotropy using group theory

Monoclinic bulk GaTe belongs to the C_{2h}^3 (*C2/m*) space group. The high symmetry points ***Γ***, ***Z*** and ***P*** in the Brillouin zone have the same C_{2h}^3 (*C2/m*) symmetry. As discussed in the main text, the direct energy bandgap occurs at the ***Z*** point and the gap energy is similar to that at the ***P*** point. Therefore we can discuss the selection rules of optical transitions near the gap energy by group theory analysis at the ***Z*** and ***P*** points in the Brillouin zone. We applied the projection operators of each irreducible representation for the C_{2h}^3 space group (Table S3) to the wave functions and determined the symmetry of

the eigenfunction for each energy band at the ***Z*** and ***P*** points. Figure 4(a) shows the selection rules of optical transitions near the Fermi energy. Details of the symmetry assignment for the energy bands are given in Figure S9. These optical transitions follow the optical selection rules of the C_{2h}^3 space group shown in Table S4. As shown in Table S4, the transitions between the A_g and B_u states and between the A_u and B_g states occur with ***x***-polarized light, while the transitions between the A_g and A_u states and between the B_g and B_u states occur with ***y***-polarized light. The main contribution near the gap energy comes from the ***x***-polarized light, and as the photon energy increases, the ***y***-polarized light is absorbed. Thus the anisotropy of the optical absorption and extinction becomes weak with increasing photon energy.

3. Analysis of Raman anisotropy using group theory

With the selection rules of optical transitions, we can explain the first-order polarization dependence presented in Table 1, Figures 2, S4, S5 and S7. The Raman intensity can be obtained by incorporating two electron-photon matrix elements with one electron-phonon matrix element as follows:[3]

$$I_v(E_L) = \left|\sum_{i,m,m'} \frac{\langle f|H_{\mathrm{op}}|m'\rangle\langle m'|H_{\mathrm{ep}}^v|m\rangle\langle m|H_{\mathrm{op}}|i\rangle}{(E_L-\Delta E_{mi})(E_L-\hbar\omega_v-\Delta E_{m'i})}\right|^2 \qquad \text{(S3)}$$

where $\Delta E_{mi} = E_m - E_i - \mathrm{i}\Gamma$, m (m') is the intermediate state and Γ is a broadening factor corresponding to the life time of the photo-excited carriers. The initial (i) and final (f) states in Eq. (S3) are the same in a Raman process. In the optical absorption and Raman spectra, finite values of the electron-photon matrix elements can be obtained when the direction of D_{mi} is not perpendicular to the light polarization direction *P* from Eq. (S1). Here, we neglect the polarization dependence of the electron-phonon matrix element $\langle m'|H_{\mathrm{ep}}^v|m\rangle$ for simplicity and thus the polarization dependence of the Raman intensity can be described by the product of two electron-photon matrix elements. We show the selection rules for the A_g and B_g Raman modes in Tables S5 and S6, respectively, and an example of the transition corresponding to the A_g and B_g modes at

the $\boldsymbol{P}$ point in Figures S10(b-c). For the A_g mode, the m and m' states have the same symmetry, and both electron-photon interaction matrices in Eq. (S3) have the same polarization dependence that gives a 180° period for the A_g polarization profile; while for the B_g mode, the m and m' states have different symmetries, and the two electron-photon interaction matrices have the opposite polarization dependences, resulting in the 90° period of the B_g polarization profiles as shown in Table 1. We can see that the calculated results well reproduce the shape of the polarization dependence of the Raman spectra found in the experiment.

4. Calculation of the interference effect

The interference effect in the sample and substrate contributes to the dependence of the observed optical extinction and Raman scattering on thickness of the sample and wavelength of the laser. We evaluate the interference effect by calculating the transmission probability with use of the transfer matrix method for the optical absorption/extinction and the enhancement factor for Raman scattering.[4–6] The refractive indices of the substrates as a function of the wavelength are adopted from Malitson, *et al.* (SiO_2)[7] and Vuye, *et al.* (Si),[8] which are listed in Table S7.

For the optical absorption of GaTe, we consider the setup of the experiment with the GaTe sample on a $d_2 = 0.5$ mm quartz substrate (Figure S11(a)) and we calculate the reflection, transmission, and absorption probabilities ($R, T,$ and A) by the transfer matrix method, as shown below. We assume the electromagnetic wave oscillating with a frequency ω and we obtain the relation between the electric and magnetic field from the Maxwell equation $\nabla \times E = -\mu_0 \frac{\partial H}{\partial t}$:

$$i\omega\mu_0 H_{i,x}(z) = -\frac{\partial E_{i,y}(z)}{\partial z} \qquad \text{(S4)}$$

where $\boldsymbol{x}$ and $\boldsymbol{y}$ are the in-plane directions, $\boldsymbol{z}$ is the direction perpendicular to the substrate layer, and μ_0 is the magnetic permeability in vacuum. The electric field in the i-th medium at the position of z is written as

$$E_{i,y}(z) = E_{i,+}e^{-ik_{i,z}(z-L_i)} + E_{i,-}e^{ik_{i,z}(z-L_i)} \qquad \text{(S5)}$$

where $E_{i,+}$ ($E_{i,-}$) is the amplitude of the electric field propagating in the +z (-z) direction and $L_i = \sum_{u=1}^{i-1} d_u$ in which d_u is the thickness of the u-th medium. From Eqs. (S4) and (S5), we can also obtain the expression for the magnetic field as

$$H_{i,x}(z) = -\Gamma_i\left(-E_{i,+}e^{-ik_{i,z}(z-L_i)} + E_{i,-}e^{ik_{i,z}(z-L_i)}\right) \qquad \text{(S6)}$$

where $\Gamma_i = \frac{k_{i,z}}{\omega\mu_0} = n_i\sqrt{\frac{\varepsilon_0}{\mu_0}}$. Using $E_{i,y}(L_i)$ and $H_{i,x}(L_i)$, E_+ and E_- are written as

$$E_{i,+} = \frac{1}{2}\left(E_{i,y}(L_i) + \frac{H_{i,x}(L_i)}{\Gamma_i}\right), \text{ and } E_{i,-} = \frac{1}{2}\left(E_{i,y}(L_i) - \frac{H_{i,x}(L_i)}{\Gamma_i}\right) \qquad \text{(S7)}$$

Using Eqs. (S5), (S6) and (S7), we can obtain the conditions of propagating the fields in the i-th medium ($L_i < z < L_{i+1}$) as follows:

$$\begin{pmatrix} E_{i,y}(z) \\ H_{i,x}(z) \end{pmatrix}$$

$$= \begin{pmatrix} \frac{1}{2}\left(e^{-ik_{i,z}(z-L_i)} + e^{ik_{i,z}(z-L_i)}\right) & \frac{1}{2\Gamma_i}\left(e^{-ik_{i,z}(z-L_i)} - e^{ik_{i,z}(z-L_i)}\right) \\ \frac{\Gamma_i}{2}\left(e^{-ik_{i,z}(z-L_i)} - e^{ik_{i,z}(z-L_i)}\right) & \frac{1}{2}\left(e^{-ik_{i,z}(z-L_i)} + e^{ik_{i,z}(z-L_i)}\right) \end{pmatrix} \begin{pmatrix} E_{i,y}(L_i) \\ H_{i,x}(L_i) \end{pmatrix} \qquad \text{(S8)}$$

Further, when we use the boundary conditions for $E_{i,y}$ and $H_{i,x}$ that are $E_{i,y}(L_i) = E_{i+1,y}(L_i)$ and $H_{i,x}(L_i) = H_{i+1,x}(L_i)$, the transfer matrix of the boundary conditions becomes an identity matrix. Therefore the relations of $E_{i,y}$ and $H_{i,x}$ between the depth at $z = L_i$ and $z = L_{i+1}$ are given by

$$\begin{pmatrix} E_{i,y}(L_{i+1}) \\ H_{i,x}(L_{i+1}) \end{pmatrix}$$

$$= \begin{pmatrix} \frac{1}{2}\left(e^{-ik_{i,z}(L_{i+1}-L_i)} + e^{ik_{i,z}(L_{i+1}-L_i)}\right) & \frac{1}{2\Gamma_i}\left(e^{-ik_{i,z}(L_{i+1}-L_i)} - e^{ik_{i,z}(L_{i+1}-L_i)}\right) \\ \frac{\Gamma_i}{2}\left(e^{-ik_{i,z}(L_{i+1}-L_i)} - e^{ik_{i,z}(L_{i+1}-L_i)}\right) & \frac{1}{2}\left(e^{-ik_{i,z}(L_{i+1}-L_i)} + e^{ik_{i,z}(L_{i+1}-L_i)}\right) \end{pmatrix} \begin{pmatrix} E_{i,y}(L_i) \\ H_{i,x}(L_i) \end{pmatrix}$$

$$= \mathcal{M}_i \begin{pmatrix} E_{i,y}(L_i) \\ H_{i,x}(L_i) \end{pmatrix} \qquad \text{(S9)}$$

Using the relations of Eq. (S9) repeatedly, we can obtain the relations for $E_{i,y}$ and $H_{i,x}$ between the depth at $z = 0$ and $z = L$ as follows:

$$\begin{pmatrix} E_{0,y}(0) \\ H_{0,x}(0) \end{pmatrix} = \mathcal{M}_1^{-1}\mathcal{M}_2^{-1}\begin{pmatrix} E_{3,y}(L) \\ H_{3,x}(L) \end{pmatrix}, \qquad \text{(S10)}$$

where $\mathcal{M} = \mathcal{M}_1^{-1}\mathcal{M}_2^{-1}$ is the transfer matrix. The reflection and transmission coefficients, r and t, are associated with $E_{i,+}$ and $E_{i,-}$ as follows:

$$r = \frac{E_{0,-}}{E_{0,+}}, t = \frac{E_{3,+}}{E_{0,+}} \qquad \text{(S11)}$$

Using Eq. (S11), we can obtain the expression for r and t as follows:

$$r = \frac{M_{11}\Gamma_0 + M_{12}\Gamma_0\Gamma_3 - M_{21} - M_{22}\Gamma_3}{M_{11}\Gamma_0 + M_{12}\Gamma_0\Gamma_3 + M_{21} + M_{22}\Gamma_3}, t = \frac{2\Gamma_0}{M_{11}\Gamma_0 + M_{12}\Gamma_0\Gamma_3 + M_{21} + M_{22}\Gamma_3} \qquad \text{(S12)}$$

where M_{ij} means the i,j component of the transfer matrix $\mathcal{M}_{ij}$. Finally, the reflection, transmission, and absorption probabilities ($A, R,$ and T) are given by

$$R = |r|^2, T = |t|^2, A = 1 - R - T \qquad \text{(S13)}$$

In order to calculate the absorption probability by the transfer matrix method, we need to obtain the complex refractive index of GaTe. We calculate the refractive index by a first-principles calculation, and also by fitting with the experimental extinction spectra to the Drude-Lorentz model;

$$\varepsilon' = 1 - \frac{{\omega_p}^2\left({\omega^2 - {\omega_0}^2}\right)^2}{(\omega^2 - {\omega_0}^2)^2 + (\omega/\tau)^2}, \text{ and } \varepsilon'' = \frac{{\omega_p}^2(\omega/\tau)}{(\omega^2 - {\omega_0}^2)^2 + (\omega/\tau)^2} \qquad \text{(S14)}$$

where ε' and ε'' are the real and imaginary parts of dielectric function, respectively. Here $\hbar\omega$ corresponds to the laser energy. The refractive index can be obtained by the relation:

$$n = \sqrt{\frac{\sqrt{{\varepsilon'}^2 + {\varepsilon''}^2} + \varepsilon'}{2}}, \text{ and } \kappa = \sqrt{\frac{\sqrt{{\varepsilon'}^2 + {\varepsilon''}^2} - \varepsilon'}{2}} + \frac{I}{\sqrt{2\pi}\sigma}\exp\left(-\frac{(\hbar\omega - E_0)^2}{2\sigma^2}\right). \qquad \text{(S15)}$$

We take into account the term $\frac{I}{\sqrt{2\pi}\sigma}\exp\left(-\frac{(\hbar\omega - E_0)^2}{2\sigma^2}\right)$ in κ in order to describe the absorption by the exciton. In order to reproduce the experiments, we fit with the experiments and determine the parameters: $\omega_0, \omega_p, \tau, I, \sigma,$ and E_0. We thus obtain the parameter as: $\hbar\omega_0 = 3.6$ eV, $\hbar\omega_p = 10.2$ eV, $\tau/\hbar = 2.7$ eV^{-1}, $I = 0.17$ eV, $\sigma = 0.20$ eV, and $E_0 = 1.62$ eV for $\boldsymbol{x}$- (0°) polarized light, and $\hbar\omega_0 = 3.8$ eV, $\hbar\omega_p = 11.0$ eV, $\tau/\hbar = 2.7$ eV^{-1}, $I = 0.14$ eV, $\sigma = 0.18$ eV, and $E_0 = 1.66$ eV for $\boldsymbol{y}$- (90°) polarized light. In Figure S11(b), we show the calculated optical absorption probability using the refractive index from the first-principles calculation. The absorption probability oscillates with wavelength and GaTe thickness due to the interference effect. In Figure S11(c), we show the optical extinction spectra obtained by the Drude-Lorentz model with

the above fitting parameters. In order to compare with experiment directly, we evaluate the optical extinction $\ln(T_{\text{substrate}}/T)$, where T and $T_{\text{substrate}}$ are the transmission probability of the sample with the substrate, and only the substrate, respectively. From the fitted calculation result, we conclude that the peak at 530 nm is given by an interference effect and the peak at 730 nm is given by the absorption in GaTe.

For the observation of Raman scattering, we consider the same situation with the experiment that the GaTe sample is on the Si/SiO_2 (300 nm) substrate (Figure S12(a)). The amplitude of the excitation light at the depth z from the top of sample is given by

$$F_{ex} = t_{01}\frac{\left(1 + r_{12}r_{23}e^{-2i\beta_2}\right)e^{-i\beta_z} + \left(r_{12} + r_{23}e^{-2i\beta_2}\right)e^{-2i(\beta_1-\beta_z)}}{1 + r_{12}r_{23}e^{-2i\beta_2} + (r_{12} + r_{23}e^{-2i\beta_2})r_{01}e^{-2i\beta_1}}, \qquad \text{(S16)}$$

where $t_{ij} = 2\tilde{n}_i/(\tilde{n}_i + \tilde{n}_j)$ and $r_{ij} = (\tilde{n}_i - \tilde{n}_j)/(\tilde{n}_i + \tilde{n}_j)$ are the Fresnel transmittance and reflection coefficients at the interfaces between the *i*-th and *j*-th medium with complex refractive indices $\tilde{n}_i$ and $\tilde{n}_j$. $\beta_i = 2\pi d_i\tilde{n}_i/\lambda$ and $\beta_z = 2\pi z\tilde{n}_1/\lambda$ are the phase factors with the wavelength of the incident light λ and the thickness of the *i*-th medium d_i. We obtain the complex refractive index of GaTe from the first-principles calculation. The amplitude of the Raman scattered light at the depth z in GaTe sample is given by

$$F_{sc} = t_{10}\frac{\left(1 + r_{12}r_{23}e^{-2i\beta_2}\right)e^{-i\beta_z} + \left(r_{12} + r_{23}e^{-2i\beta_2}\right)e^{-2i(\beta_1-\beta_z)}}{1 + r_{12}r_{23}e^{-2i\beta_2} + (r_{12} + r_{23}e^{-2i\beta_2})r_{01}e^{-2i\beta_1}}. \qquad \text{(S17)}$$

We can assume that β_i is the same for F_{ex} and F_{sc} since the wavenumber of the scattered light is almost the same as the incident light. Actually, the Raman shift of GaTe observed in this experiment is smaller than 300 cm^{-1}. The total enhancement factor F is written as follows:

$$F = \int_0^{d_1} |F_{ex} \cdot F_{sc}|^2 \, dz, \qquad \text{(S18)}$$

and the total Raman intensity I is written as $I = I_i \cdot F$, with the intrinsic Raman intensity denoted by I_i. In the calculation of the enhancement factor, we use the refractive index obtained from the first-principles calculation. Figures S12(b-d) are the GaTe thickness dependence of the calculated enhancement factor. As seen in Figure S12(b), which shows the calculated ratio of the enhancement factors in the ***x***- and ***y***-directions for the Raman intensity, the interference effect causes the Raman intensity in the ***x***-direction to be

smaller than in the ***y***-direction for both excitation wavelengths 532 and 633 nm, and almost the same intensity in the ***x*** and ***y***-directions for the wavelength 785 nm. These differ from the experimental observations (Table 1), suggesting that the anisotropy of the Raman intensity cannot be mainly attributed to the interference effect, but is mostly due to the anisotropy of the light-matter interactions.

5. Supporting figures and tables

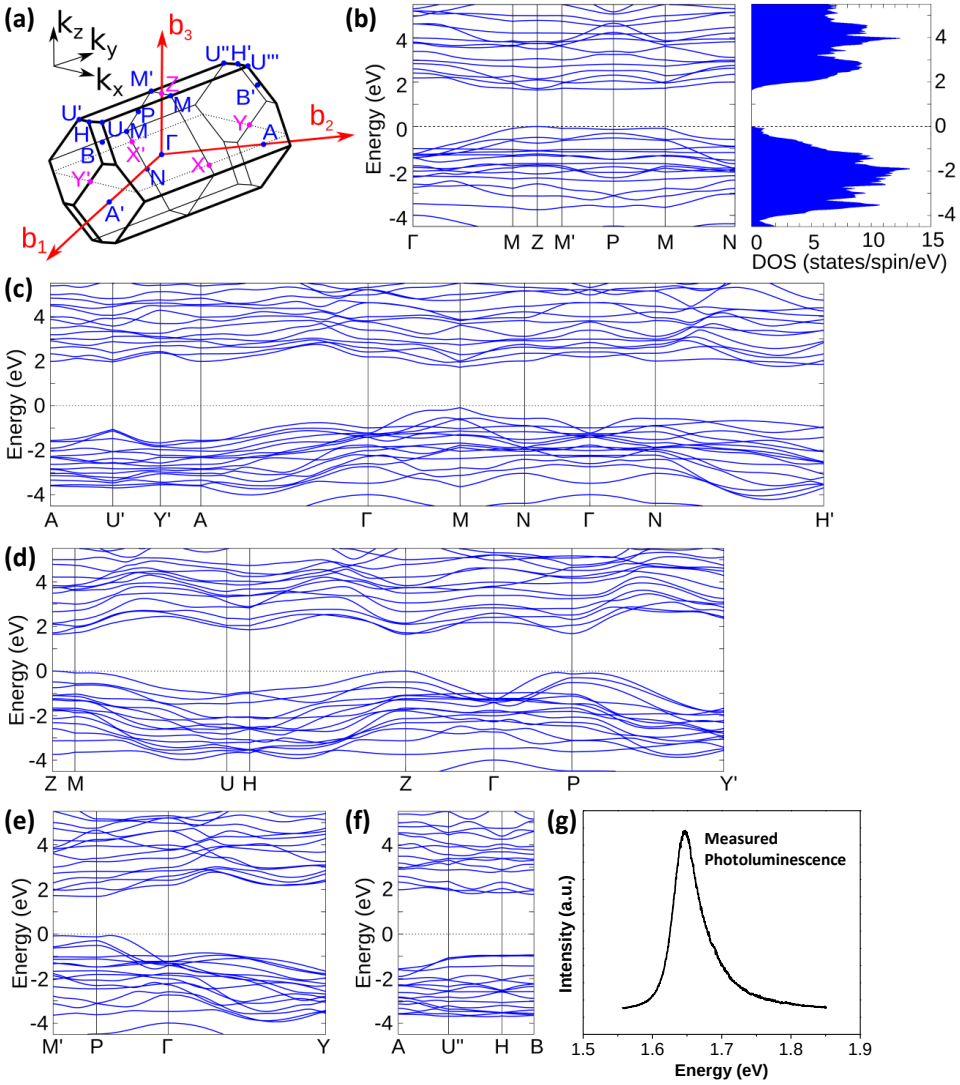

Figure S1. Electronic energy bands of bulk-GaTe. The maximum energy of the valence band at the ***Z*** point is set to zero. (a) The first Brillouin zone of GaTe showing high symmetry points. (b-f) are the energy band structures along the high-symmetry lines obtained from density functional theory (DFT) calculations. The right panel of (b) shows the density of states. (g) Measured photoluminescence spectrum of a GaTe flake with a thickness of 152 nm. The peak position is at 1.65 eV. The excitation laser wavelength is 532 nm, and the measurement was performed at room temperature. There is a direct energy bandgap at the ***Z*** point and similar bandgaps around the ***P***, ***M***, and ***M'*** points. Conduction bands are upshifted by 0.7 eV due to the underestimation of the energy gap

from the DFT calculation; thus we adjust the energy bands according to the peak position of the photoluminescence spectrum in (g).

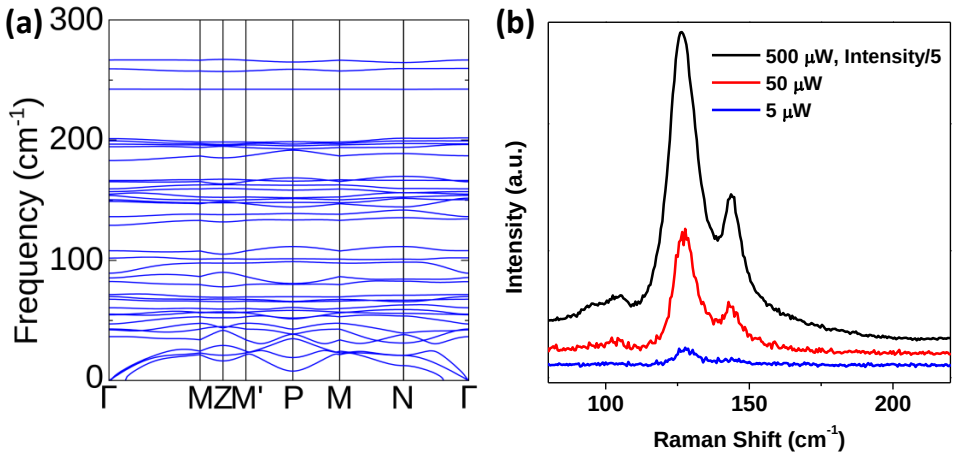

Figure S2. (a) The phonon dispersion relations of bulk GaTe along the ***Γ*–*M*–*Z*–*M'*–*P*–*M*–*N*–*Γ*** line calculated by the density functional perturbation theory (DFPT) method. From the dispersion relations, we obtained the phonon frequencies at the ***Γ*** point to assign the Raman peaks. The calculated frequency values and vibrational motions of all the phonon modes at the ***Γ*** point are listed in Table S1 and Figure S3, respectively. (b) The excitation laser power dependence of the measured Raman intensity. The Raman spectra were measured on a GaTe flake under 532 nm laser excitation with three different power levels: 500, 50 and 5 μW. The spectrum with 500 μW excitation laser power is shown with 1/5 the measured intensity. The intensities of the peaks at 126 cm^{-1} and 142 cm^{-1} are proportional to the laser power.

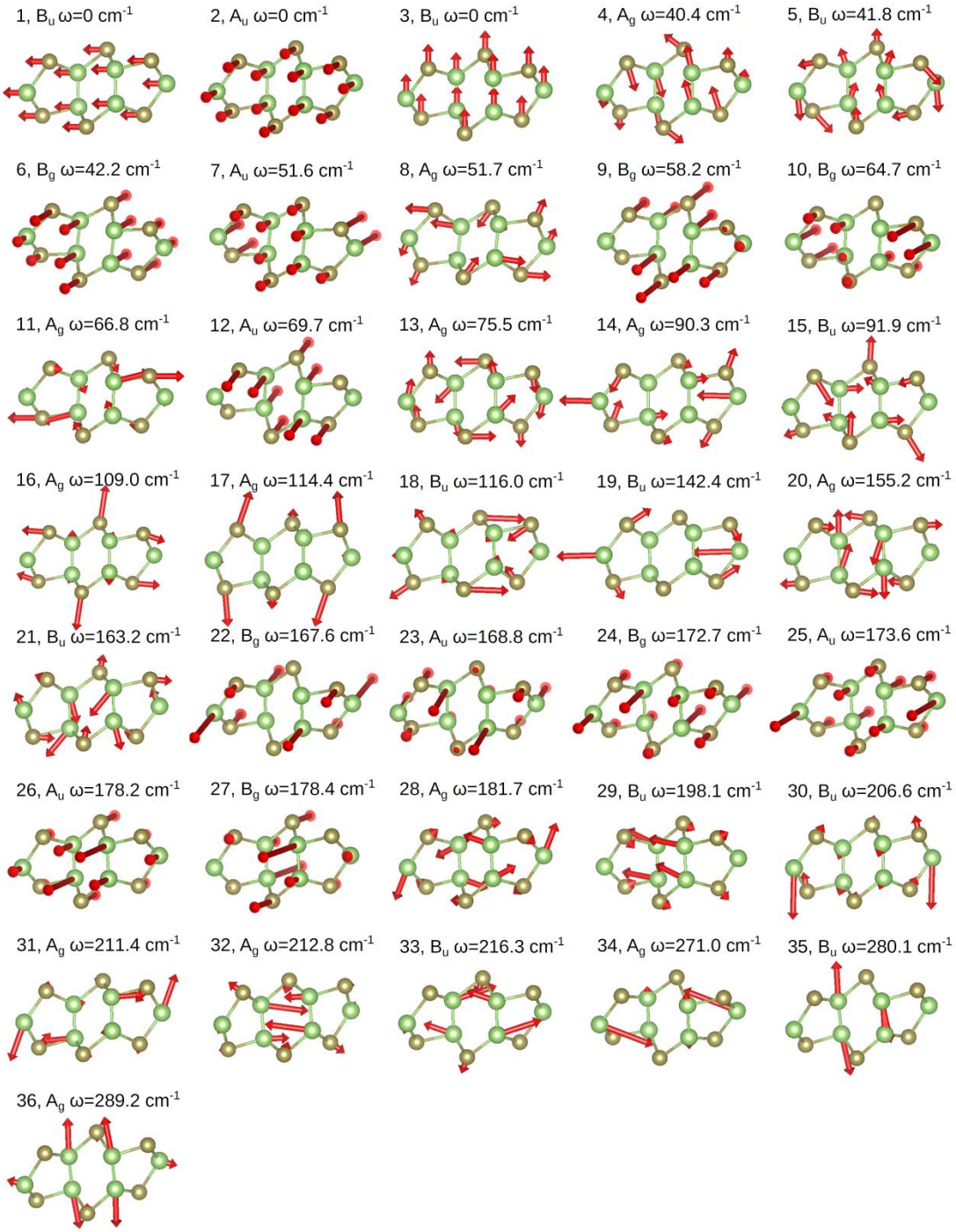

Figure S3. Illustration of the atomic vibrational motions of the phonon modes at the ***Γ*** point in bulk GaTe. See Table S1 for assignment of phonon modes.

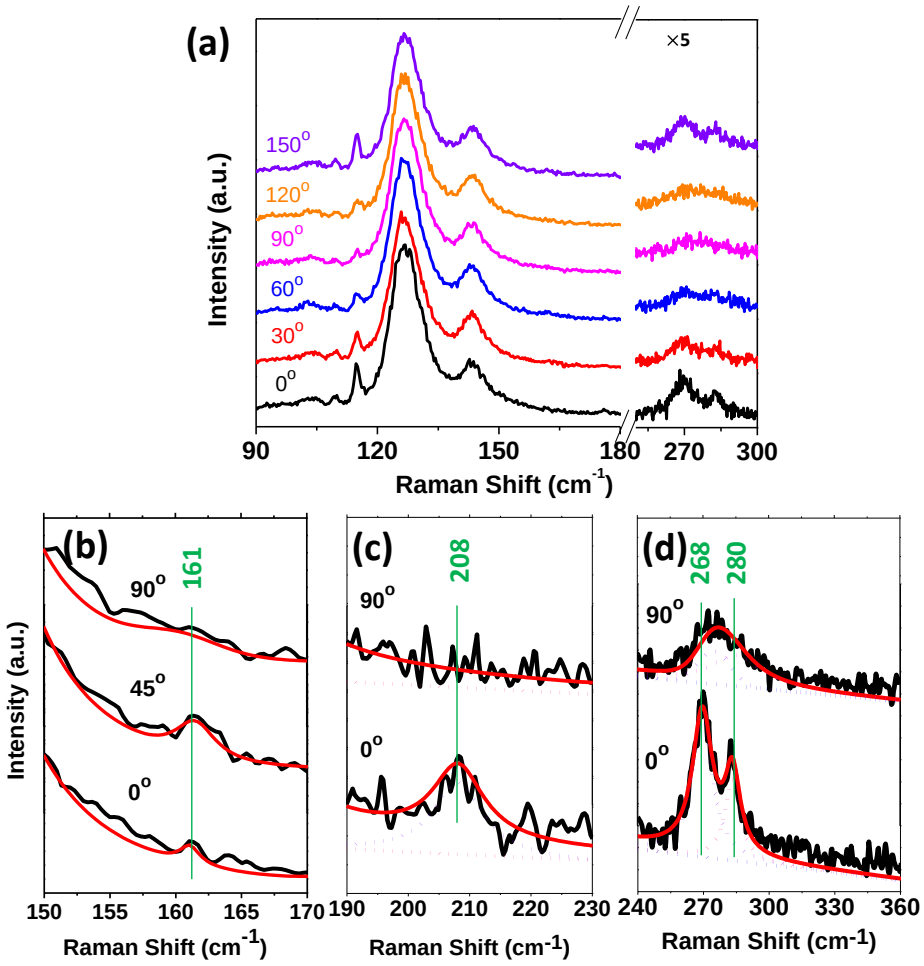

Figure S4. (a) Experimental Raman spectra of the GaTe flake in Figure 2(a) at different polarization angles from 0° to 150° with the excitation wavelength of 633 nm. (b-d) show in more detail the peak fittings and peak frequencies (in units of cm^{-1}). (b-d) show different spectral ranges.

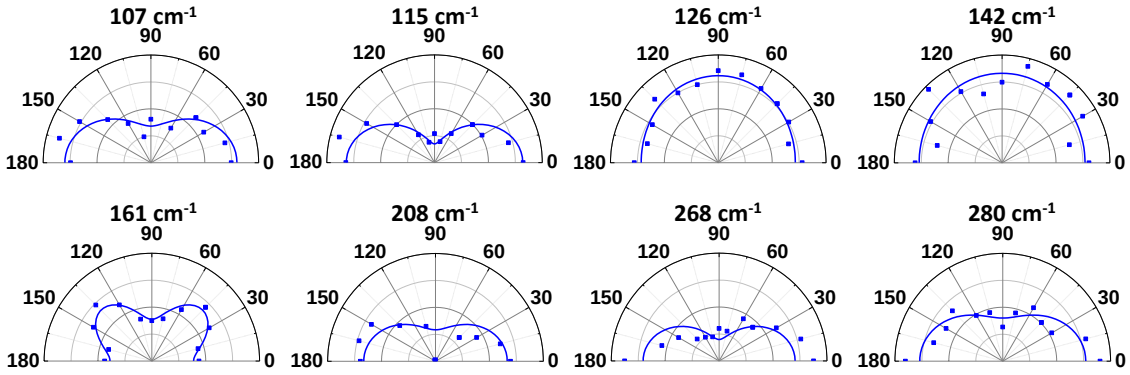

Figure S5. The Raman intensity vs. polarization angle for eight Raman modes on the same GaTe flake as shown in Figure 2. The squares are experimental values and the curves are numerical fittings. The Raman shift values are labeled above each panel. 0° (90°) corresponds to the ***x***- (***y***-) axis of the GaTe crystal.

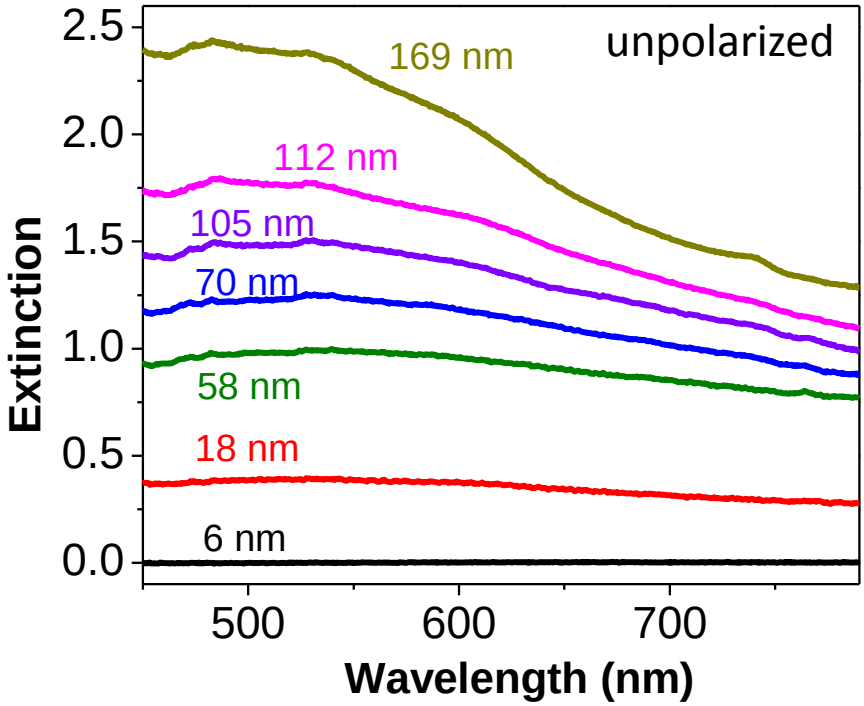

Figure S6. Non-polarized optical extinction spectra of GaTe flakes with thicknesses from 6 to 169 nm, which are labeled and color coded beside the corresponding spectra.

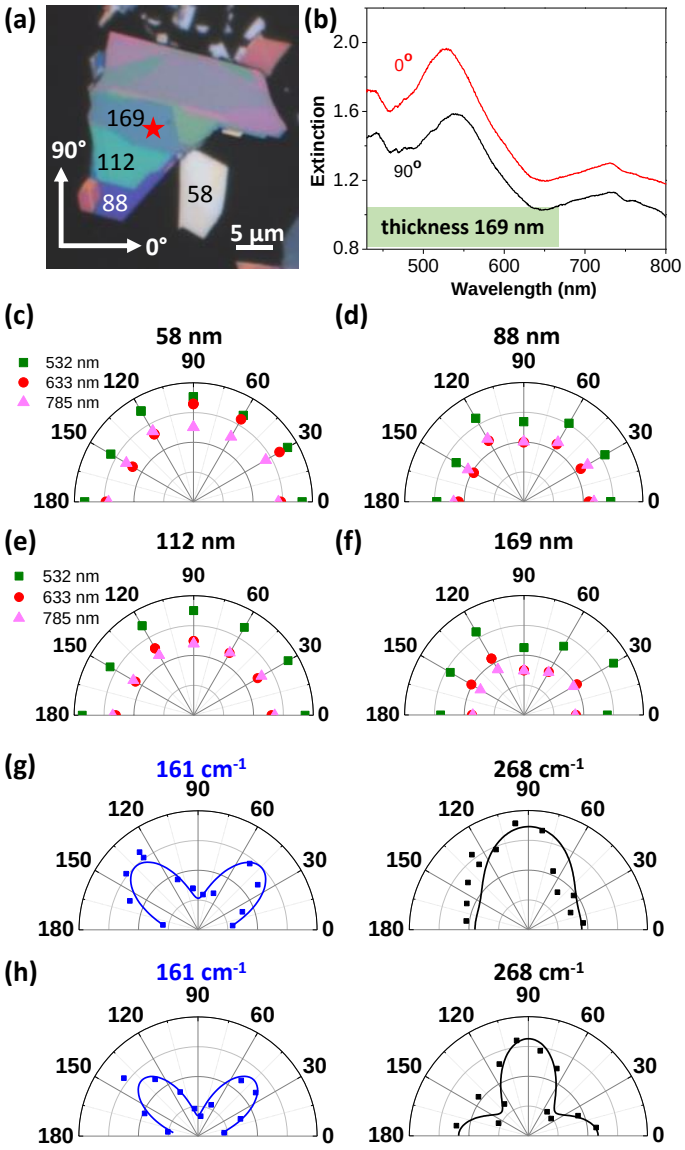

Figure S7. Polarized optical extinction and Raman spectra of GaTe. (a) The optical microscope image (same as Figure 3(a)) of the four flakes (the thicknesses are labeled in units of nm). The flakes have the same crystalline orientation, because they are physically connected to each other and are exfoliated from the same single-crystal bulk. (b) Polarized optical extinction spectra of the 169 nm-thick flake (labeled with a star in (a)) measured with incident light polarized at 0^{o} and 90^{o}. (c-f) The extinction at wavelengths 532, 633 and 785 nm with different polarization angles for flakes with thicknesses of 58, 88, 112 and 169 nm, respectively. (g-h) The polarized Raman peak intensity of the 169

nm-thick flake (g) and the 112 nm-thick flake (h) for Raman modes 161 cm^{-1} and 268 cm^{-1}. The excitation wavelength is 532 nm. The squares are experimental values and the curves are numerical fittings. The polarization angle corresponds to the angular coordinates in (a). Using the polarized Raman (g-h), we can determine that the 0° (90°) orientations in (a) and Figure 3(a) correspond to ***x***- (***y***-) axis as below. Here the excitation wavelength is 532 nm, under which the anisotropy of the 268 cm^{-1} mode with the major (secondary) maximum axis is along the ***y***- (***x***-) axis of the GaTe crystal, while the minimum values of the 161 cm^{-1} mode are along both ***x***- and ***y***-axes (Table 1). Therefore, from the polarization dependence of the Raman spectra, we can identify the crystalline orientation: for the flakes in (a) and in Figure 3 in the main text, the 0° and 90° orientations correspond to the ***x***- and ***y***-axes, respectively.

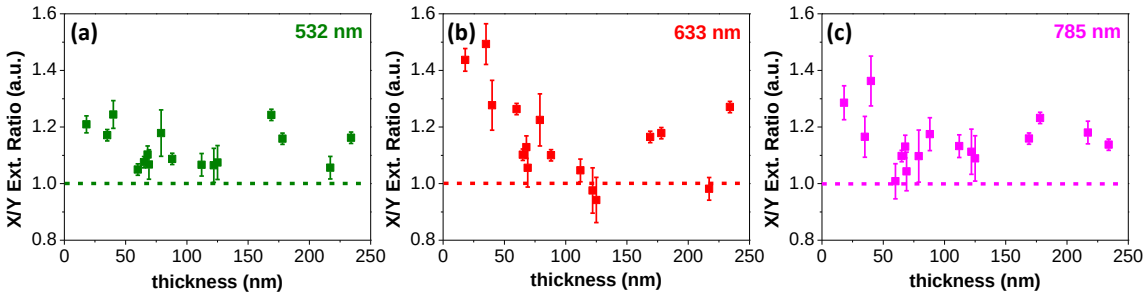

Figure S8. Thickness dependence of the extinction ratio of ***x***- and ***y***- polarized light. (a-c) show the optical extinction ratio at wavelengths 532, 633 and 785 nm, respectively. Dashed horizontal lines indicate the extinction ratio equals 1.0 (isotropic).

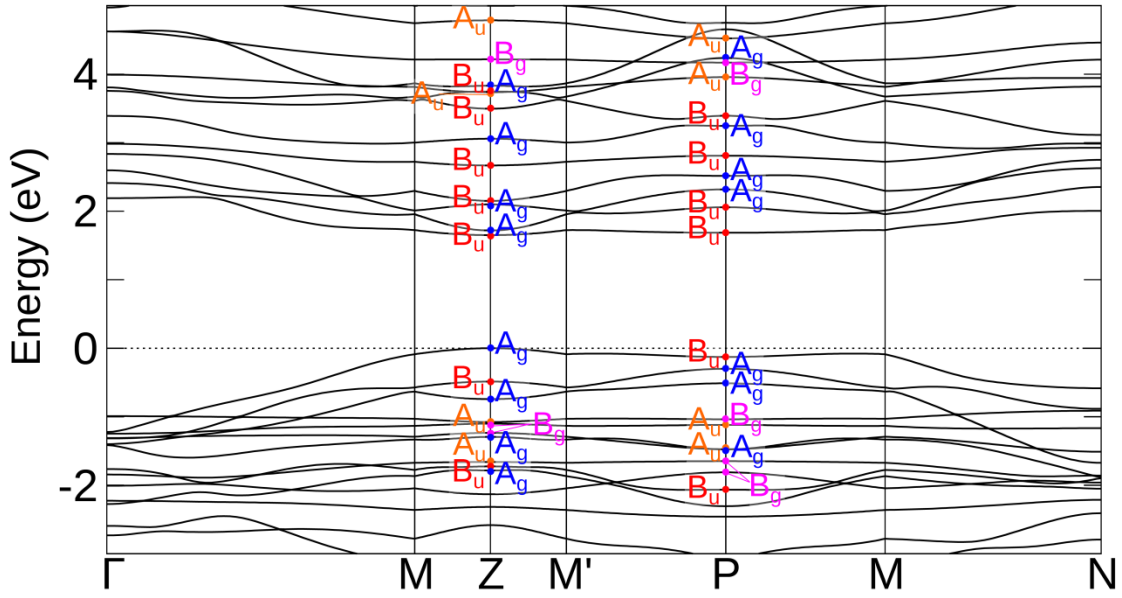

Figure S9. Symmetry assignment of the electronic energy bands of bulk GaTe at the ***Z*** and ***P*** points in the Brillouin zone. Different colors indicate different symmetries.

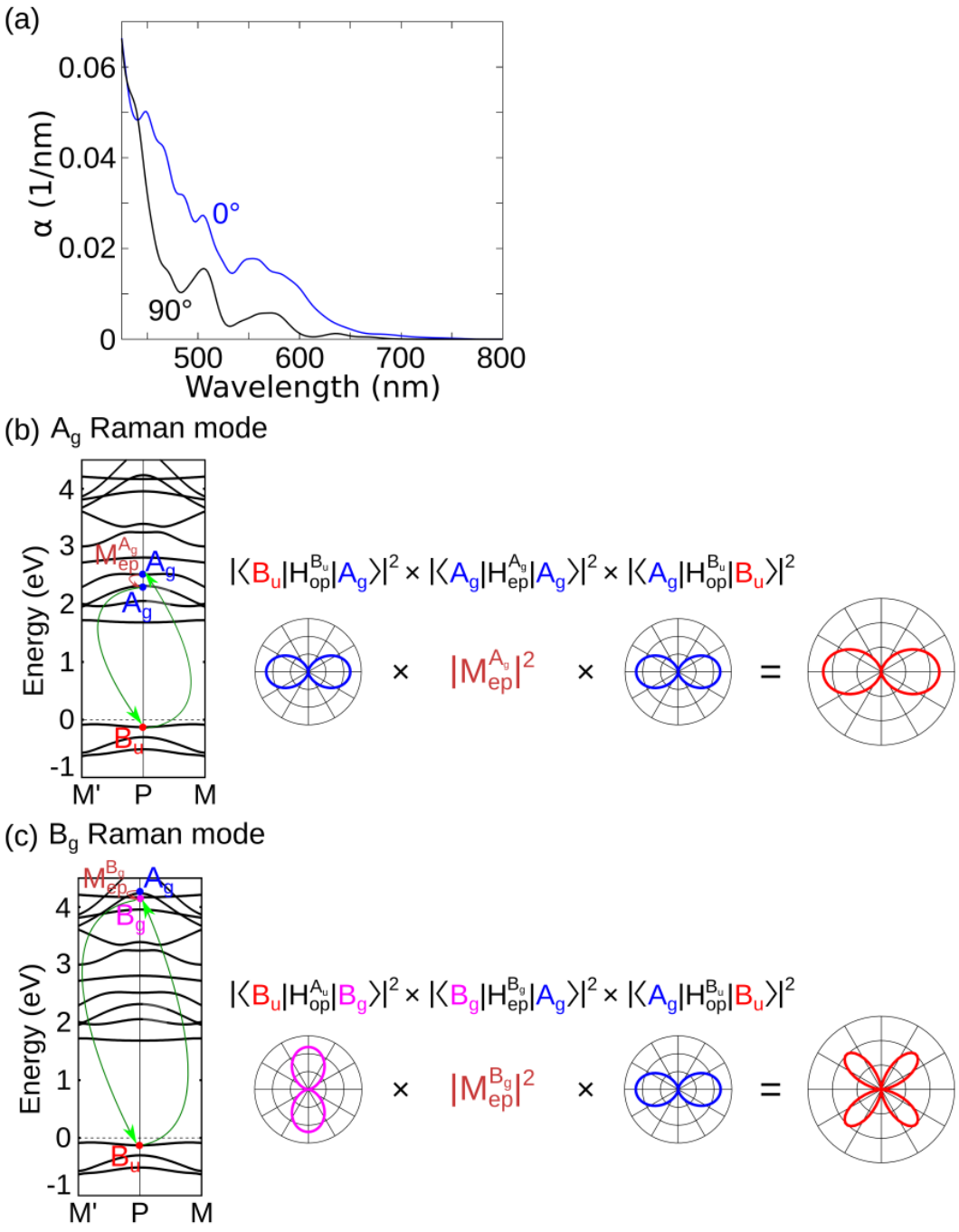

Figure S10. (a) Absorption spectrum of bulk GaTe for ***x***- (0°) and ***y***- (90°) polarized light calculated from the electron-photon matrix elements obtained by our first-principles calculation. (b-c) One of the expected transitions for Raman scattering and the expected polarization shape for the A_g (b) and B_g (c) modes at the ***P*** point. $M_{\mathrm{ep}}^{A_g}$ ($M_{\mathrm{ep}}^{B_g}$) indicates the electron-phonon interaction emitting an A_g (B_g) phonon.

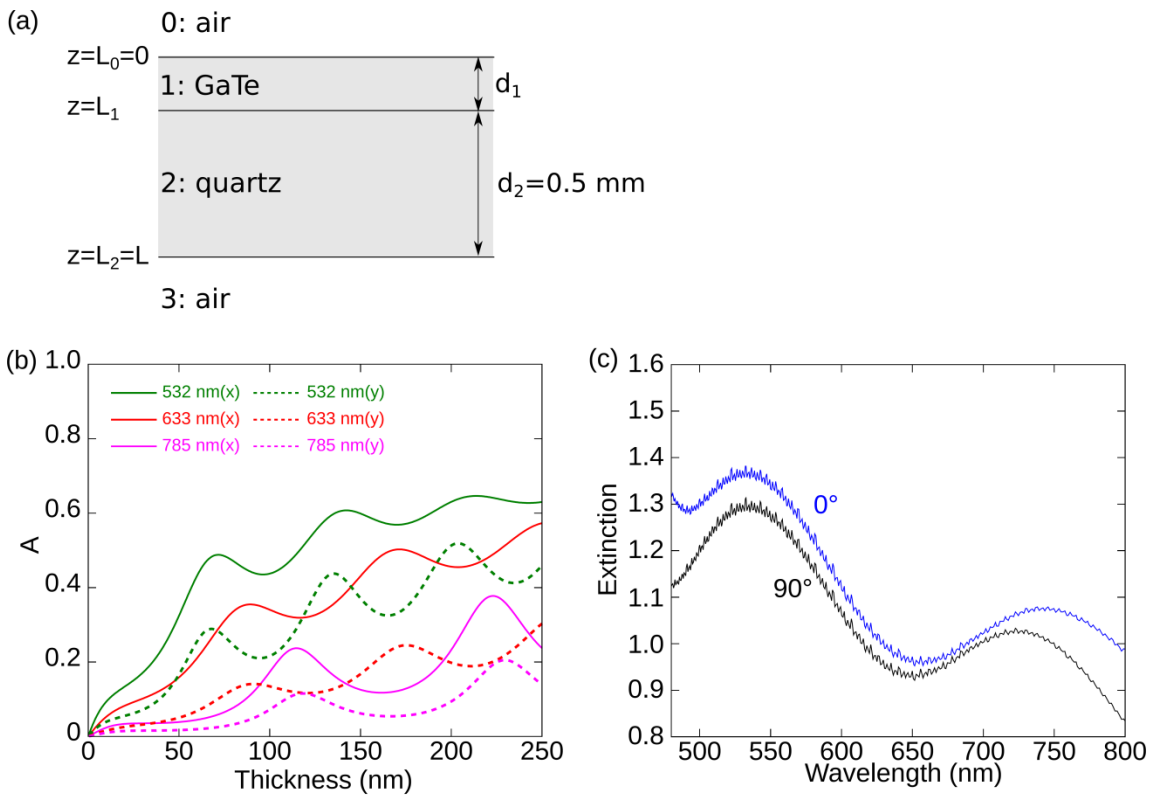

Figure S11. Calculated results for the interference effect for the optical absorption and extinction. (a) Geometrical arrangement of the experiment. (b) GaTe thickness dependence of the calculated optical absorption probability for ***x***- (solid line) and ***y***- (dashed line) polarized light. The results for the three laser energies (532, 633 and 785 nm) are shown. We use the complex refractive index obtained from the first-principles calculation (Table S7) whose energy dependence is shifted by 0.7 eV in order to be consistent with the experiment. (c) Calculated optical extinction, fitted to the experiment of the 112 nm-thick sample (Figure 3(b) in the main text) with the Drude-Lorentz model including the exciton absorption term.

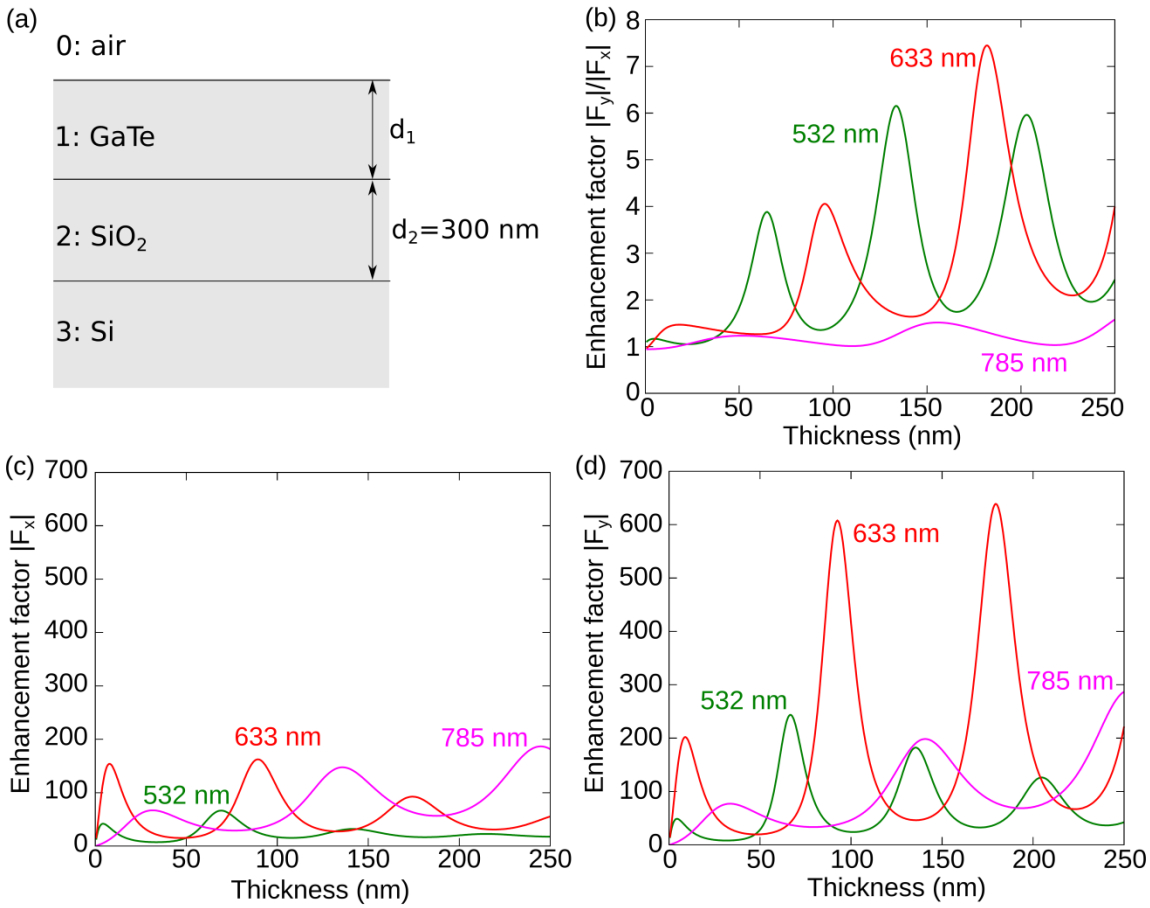

Figure S12. Calculated results for the enhancement factor for the interference effect on the Raman intensity. (a) Geometrical arrangement of the experiment. (b) The ratio of the enhancement factor for ***x***- and ***y***-polarized light as a function of GaTe thickness. (c-d) GaTe thickness dependence of the enhancement factor for ***x***- (c) and ***y***- (d) polarized light. Calculated results for the three laser wavelengths (532, 633 and 785 nm) are shown.

Table S1. Calculated Γ point phonon and assignments with experiment. Blue and red colors are Raman-active A_g and B_g modes, respectively. Black color shows the Raman-inactive modes. The labeled number of each phonon mode corresponds to the illustration in Figure S3. "Calc." and "Exp." show the calculated and experimental values of phonon frequencies, respectively.

	Calc. (cm^{-1})	Symmetry	Exp. (cm^{-1})		Calc. (cm^{-1})	Symmetry	Exp. (cm^{-1})
1	0	B_u		19	142.4	B_u	
2	0	A_u		20	155.2	A_g	
3	0	B_u		21	163.2	B_u	
4	40.4	A_g		22	167.6	B_g	161
5	41.8	B_u		23	168.8	A_u	
6	42.2	B_g		24	172.7	B_g	
7	51.6	A_u		25	173.6	A_u	
8	51.7	A_g		26	178.2	A_u	
9	58.2	B_g		27	178.4	B_g	
10	64.7	B_g		28	181.7	A_g	
11	66.8	A_g		29	198.1	B_u	
12	69.7	A_u		30	206.6	B_u	
13	75.5	A_g		31	211.4	A_g	208
14	90.3	B_u		32	212.8	A_g	208
15	91.9	B_u		33	216.3	B_u	
16	109.0	A_g	107	34	271.0	A_g	268
17	114.4	A_g	115	35	280.1	B_u	
18	116.0	B_u		36	289.2	A_g	280

Table S2. The Raman anisotropy dependence on the flake thickness and laser wavelength for the two double-resonant phonon modes: 126 and 142 cm^{-1}. The Raman intensity polar plots for the two flakes (same flakes as in Table 1) with different thicknesses: 58 and 136 nm, are shown here. These two flakes have the same crystalline orientation. The dots are experimental values and the curves are numerical fittings. The laser excitation wavelengths and the Raman peak frequencies are also labeled. 0° (90°) corresponds to the ***x***- (***y***-) axis of the GaTe crystal.

Laser / Peak (cm^{-1})	**532 nm**		**633 nm**		**785 nm**	
	Thin (58 nm)	Thick (136 nm)	Thin	Thick	Thin	Thick
126	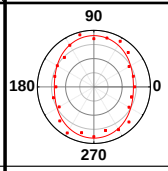	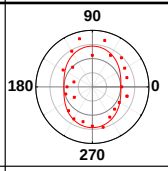	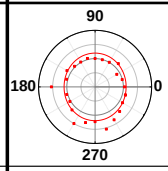	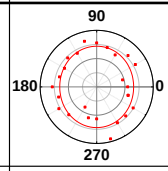	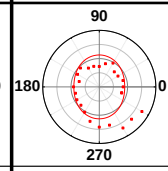	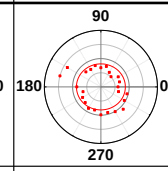
142	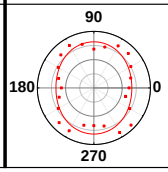	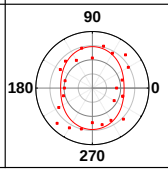	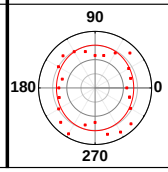	weak	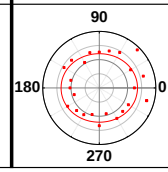	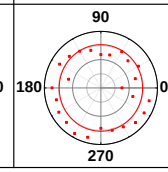

Table S3. Character table for the C_{2h}^{3} space group. $C_2(y)$ is a two-fold rotational axis along the ***y***-direction, and σ_h denotes the ***x***-***z*** mirror plane in bulk monoclinic GaTe.

C_{2h}^{3}	E	$C_2(y)$	i	σ_h	Linear functions, rotations
A_g	1	1	1	1	R_y
B_g	1	-1	1	-1	R_x, R_z
A_u	1	1	-1	-1	y
B_u	1	-1	-1	1	x, z

Table S4. Selection rules of optical transitions for the C_{2h}^{3} space group. These selection rules correspond to the electron-photon matrix element $\langle f|H_{\mathrm{op}}|i\rangle$, which is described by ∇ and is coupled by the inner product with polarization vector (Eq. (S1)).

x-polarized light $\nabla = B_u$		***y***-polarized light $\nabla = \mathrm{A}_u$	
$\|f\rangle$	$\|i\rangle$	$\|f\rangle$	$\|i\rangle$
B_u	A_g	A_u	A_g
A_u	B_g	B_u	B_g
B_g	A_u	A_g	A_u
A_g	B_u	B_g	B_u

Table S5. Selection rules of Raman scattering for the A_g mode phonon. $|i\rangle$, $|m\rangle$ and $|m'\rangle$ are the initial state and two intermediate states, respectively. ***xx*** (***yy***) are polarization vectors for the incident and scattered light: both are ***x***- (***y***-) polarized. These selection rules correspond to the product of the matrix elements: $\langle f|H_{\mathrm{op}}^{x}|m'\rangle\langle m'|H_{\mathrm{ep}}(A_g)|m\rangle\langle m|H_{\mathrm{op}}^{x}|i\rangle$ and $\langle f|H_{\mathrm{op}}^{y}|m'\rangle\langle m'|H_{\mathrm{ep}}(A_g)|m\rangle\langle m|H_{\mathrm{op}}^{y}|i\rangle$.

xx		***yy***	
$\|i\rangle = \|f\rangle$	$\|m\rangle = \|m'\rangle$	$\|i\rangle = \|f\rangle$	$\|m\rangle = \|m'\rangle$
A_g	B_u	A_g	A_u
B_g	A_u	B_g	B_u
A_u	B_g	A_u	A_g
B_u	A_g	B_u	B_g

Table S6. Selection rules of Raman scattering for the B_g mode phonon. The polarization is different for the incident and scattered light for the B_g mode. ***xy*** means that the incident light is ***y***-polarized, and the scattered light is ***x***-polarized. These selection rules correspond to the product of the matrix elements: $\langle f|H_{\mathrm{op}}^{x}|m'\rangle\langle m'|H_{\mathrm{ep}}(B_g)|m\rangle\langle m|H_{\mathrm{op}}^{y}|i\rangle$ and $\langle f|H_{\mathrm{op}}^{y}|m'\rangle\langle m'|H_{\mathrm{ep}}(B_g)|m\rangle\langle m|H_{\mathrm{op}}^{x}|i\rangle$.

xy			***yx***		
$\|i\rangle = \|f\rangle$	$\|m\rangle$	$\|m'\rangle$	$\|i\rangle = \|f\rangle$	$\|m\rangle$	$\|m'\rangle$
A_g	A_u	B_u	A_g	B_u	A_u
B_g	B_u	A_u	B_g	A_u	B_u
A_u	A_g	B_g	A_u	B_g	A_g
B_u	B_g	A_g	B_u	A_g	B_g

Table S7. Laser wavelength dependence of the complex refractive index $\tilde{n}$ of bulk GaTe for the ***x***- and ***y***- directions, SiO_2,[7] and Si.[8]

Wavelength	GaTe (***x***)	GaTe (***y***)	SiO_2	Si
532 nm	$3.70 - 0.515i$	$3.87 - 0.211i$	1.46	$4.21 - 0.010i$
633 nm	$3.74 - 0.318i$	$3.65 - 0.0926i$	1.46	$4.14 - 0.0010i$
785 nm	$3.59 - 0.0923i$	$3.49 - 0.0389i$	1.46	$4.00 - 0.0010i$

References:

(1) Sakurai, J. J.; Napolitano, J. J. *Modern Quantum Mechanics*; 2nd ed.; Addison-Wesley, 2011.

(2) Sánchez-Royo, J. F.; Segura, A.; Muñoz, V. Anisotropy of the refractive index and absorption coefficient in the layer plane of gallium telluride single crystals. *Phys. Status Solidi* **1995**, *151*, 257–265.

(3) Saito, R.; Tatsumi, Y.; Huang, S.; Ling, X.; Dresselhaus, M. S. Raman Spectroscopy of Transition Metal Dichalcogenides. *J. Phys. Condens. Matter* **2016**, *28*, 353002.

(4) Li, S.-L.; Miyazaki, H.; Song, H.; Kuramochi, H.; Nakaharai, S.; Tsukagoshi, K. Quantitative Raman Spectrum and Reliable Thickness Identification for Atomic Layers on Insulating Substrates. *ACS Nano* **2012**, *6*, 7381–7388.

(5) Yoon, D.; Moon, H.; Son, Y.-W.; Choi, J. S.; Park, B. H.; Cha, Y. H.; Kim, Y. D.; Cheong, H. Interference Effect on Raman Spectrum of Graphene on SiO2/Si. *Phys. Rev. B* **2009**, *80*, 125422.

(6) Wang, Y. Y.; Ni, Z. H.; Shen, Z. X.; Wang, H. M.; Wu, Y. H. Interference Enhancement of Raman Signal of Graphene. *Appl. Phys. Lett.* **2008**, *92*, 043121.

(7) Malitson, I. H. Interspecimen Comparison of the Refractive Index of Fused Silica. *J. Opt. Soc. Am.* **1965**, *55*, 1205.

(8) Vuye, G.; Fisson, S.; Nguyen Van, V.; Wang, Y.; Rivory, J.; Abelès, F. Temperature Dependence of the Dielectric Function of Silicon Using in Situ Spectroscopic Ellipsometry. *Thin Solid Films* **1993**, *233*, 166–170.